arXiv:astro-ph/0407026v1 1 Jul 2004

Chandra Observations and Models of the Mixed Morphology Supernova Remnant W44: Global Trends

R. L. Shelton[12], K. D. Kuntz[3], R. Petre[4]

The Department of Physics and Astronomy and the Center for Simulational Physics at the University of Georgia, Athens, GA 30602

The Department of Physics at the Univeristy University of Maryland at Baltimore County

NASA's Goddard Space Flight Center

rls@hal.physast.uga.edu

kuntz@milkyway.gsfc.nasa.gov

rob@milkyway.gsfc.nasa.gov

ABSTRACT

We report on the *Chandra* observations of the archetypical mixed morphology (or thermal composite) supernova remnant, W44. As with other mixed morphology remnants, W44's projected center is bright in thermal X-rays. It has an obvious radio shell, but no discernable X-ray shell. In addition, X-ray bright 'knots' dot W44's image. The spectral analysis of the *Chandra* data show that the remnant's hot, bright projected center is metal-rich and that the bright knots are regions of comparatively elevated elemental abundances. Neon is among the affected elements, suggesting that ejecta contributes to the abundance trends. Furthermore, some of the emitting iron atoms appear to be underionized with respect to the other ions, providing the first potential X-ray evidence for dust destruction in a supernova remnant. We use the *Chandra* data to test the following explanations for W44's X-ray bright center: 1.) entropy mixing due to bulk mixing or thermal conduction, 2.) evaporation of swept up clouds, and 3.) a metallicity gradient, possibly due to dust destruction and ejecta enrichment. In these tests, we assume that the remnant has evolved beyond the adiabatic evolutionary stage, which explains the X-ray dimness of the shell. The entropy mixed model spectrum was tested against the *Chandra* spectrum for the remnant's projected center and found to be a good match. The evaporating clouds model was constrained by the finding that the ionization parameters of the bright knots are similar to those of the surrounding regions. While both the entropy mixed and

the evaporating clouds models are known to predict centrally bright X-ray morphologies, their predictions fall short of the observed brightness gradient. The resulting brightness gap can be largely filled in by emission from the extra metals in and near the remnant's projected center. The preponderance of evidence (including that drawn from other studies) suggests that W44's remarkable morphology can be attributed to dust destruction and ejecta enrichment within an entropy mixed, adiabatic phase supernova remnant. The *Chandra* data prompts a new question – by what astrophysical mechanisms are the metals distributed so inhomogeneously in the supernova remnant.

Subject headings: ISM: individual (W44) – supernova remnants – ISM:abundances – X-rays:ISM

1. Introduction

Of the middled aged remnants, W44 is remarkably well studied. X-ray observations of this supernova remnant (SNR) reveal centrally concentrated, thermal X-ray emission (Smith et al. (1985), Jones et al. (1993), Rho et al. (1994), and Harrus et al. (1997)), while radio observations reveal a filamentary, edge brightened, elongated, synchrotron emission shell (see the beautiful radio-frequency images in Jones, Smith, and Angellini's (1993)). Because W44 has both a thermal X-ray bright center and a radio synchrotron shell, it is the epitome of 'thermal composite' or 'mixed morphology' supernova remnants. Such remnants form a puzzling class. No simple models of supernova remnants evolving in a homogeneous ambient medium can explain the tremendous fluxes of thermal X-rays emitted by the centers of these remnants. For this reason, remnants like W44 have become specimens with which to examine plasma physics, remnant evolution, and the inhomogeneous interstellar medium (ISM). Here, we follow up on such studies by examining the new *Chandra* ACIS data.

Section 2 presents a more comprehensive description of W44, including its environment, cool shell, pulsar, and X-ray characteristics. During the W44's long history as a specimen for examination, many interpretations have been suggested. These are presented in Section 3. The *Chandra* images and spectra are presented, examined, and compared with models in Section 4. Section 5 summarizes the results.

2. Summary of W44 Explorations

2.1. Setting

W44, also called 3C 392, lies in the Galactic plane, at $l = 34.7^{\rm o}$, $b = -0.4^{\rm o}$ (R.A. $= 18^{\rm h}56^{\rm m}05^{\rm s}$, dec $= 01^{\rm o}23'28''$ in (J2000) coordinates). According to Cox et al.'s (1999) calculations from the Caswell et al. (1975) 21 cm data and the Clemens (1985) Galactic rotation curves, W44 has a distance of 2.5 to 2.6 kpc. When viewed in projection, W44 appears to reside within a forest of dense clouds (Sato 1986; Dame et al. 1986). Given W44's proximity to the molecular clouds, it is not surprising that the environmental interstellar matter is thought to be relatively dense (~ 6 atoms cm^{-3}, Cox et al. (1999)).

2.2. Shell Observed in Radio-Continuum, H I, Hα, and [SII]

The first reports of W44's radio continuum emission came in 1958 (Westerhout 1958). In the course of later analyses, W44 was identified as a supernova remnant and labeled as "shell type." Although the literal interpretation of this term brings to mind a bright ring of emission, W44's radio-continuum shell is well developed only in the northeast quadrant (assuming equatorial coordinates, see figures in Jones, Smith, & Angellini (1993); Giacani et al. (1997) and this paper's Figure 1). In contrast, W44's radio continuum flux gradient is more gradual and its silhouette is more ragged in the other quadrants. Cox et al. (1999) interpreted the radio continuum morphology as that of a partially formed compressed shell. The shell is mature in the aft northeast section, but nowhere else (see Figure 1 of Cox et al. (1999)). The overall dimensions of this remnant are 25' $\times$ 35' (from Giacani et al. (1997)'s 1442.5 MHz image), the shape is elliptical or pear-like, and the semi-major axis is oriented northwest-southeast. The radio-continuum emission's spectral index is ~ 0.3 to -0.4 (Kovalenko, Pynzar', & Udal'tsov 1994; Kassim 1992; Giacani et al. 1997), indicative of radio synchrotron emission from electrons in the shocked and swept up gas at the remnant's periphery.

Part of a shell has also been observed via tracers of neutral material. Koo & Heiles (1995)'s velocity resolved H I 21 cm emission data for W44 exhibit the signature of the back (receding) side of a shell expanding at ~ 150 km sec^{-1}, leading Cox et al. (1999) to think that the shell is incomplete and more like a cap than a sphere. (For an alternate explanation, see Koo & Heiles (1995).) Furthermore, the published optical data suggest that W44 has partial shells of Hα and [SII]. In Giacani et al. (1997)'s images, [SII] outlines W44's north and west quadrants, while Hα outlines shorter segments in the north and west. In some regions the optical images correlate well with the radio emission images, as expected in gas

compressed by radiative shocks. These indications of the presence of a cool, compressed shell, work in concert with the current interpretations for W44's X-ray morphology (see section 3.1). Another intersection between the optical interpretations and the X-ray interpretations (see Section 3.2) was noted by Rho et al. (1994). Noting that the remnant's face (when viewed in projection) emits [SII] and Hα, Rho et al. (1994) suggested that if the interior of the remnant contains evaporating clouds, then the optical emission might arise from the evaporated material. However, the evaporation zones would also be expected to emit soft X-rays and there is little correlation between the soft X-ray images and the optical images.

The remnant has been successfully searched for OH 1720.53 MHz maser emission (Claussen et al. 1997) and [OI] emission (Reach & Rho 1996). These researchers suggest that these signals result from collisions between the SNR and molecular clouds, while Cox et al. (1999) suggest that they originate in the denser parts of the remnant's shell.

2.3. Pulsar Establishes W44's Age

In 1991, Wolszczan, Cordes & Dewey reported a 20,000 year old pulsar near W44's projected center and at about the same distance. This pulsar, called PSR B1853+01, and attributed to W44, appears to have a wind nebula that emits radio frequency and X-ray synchrotron photons (Harrus et al. 1996; Petre et al. 2002; Frail et al. 1996b). As seen in Petre et al. (2002)'s Figure 2 (made with this *Chandra* data), the spatial extent of the nebula's nonthermal X-ray emission region is only half an arcminute. Neither the pulsar nor its wind nebula are thought to affect the supernova remnant noticeably.

2.4. X-ray Observations Reveal W44's Unusual Characteristics

Prior to the *Chandra* era, W44 had been observed by the *Astronomical Netherlands Satellite* (*ANS*), *Einstein*, the *European X-ray Observatory Satellite* (*EXOSAT*), the *Roentgen Satellite* (*ROSAT*), and the *Advanced Satellite for Cosmology and Astrophysics* (*ASCA*) (Gronenschild et al. 1978; Szymkowiak 1980; Smith et al. 1985; Jones, Smith, & Angellini 1993; Rho et al. 1994; Harrus et al. 1996, 1997; Shelton et al. 1999). From the imaging observations, we know that the entire projected area of W44 (as defined by the radio continuum emission) is bright in X-ray emission. The X-ray surface brightness peaks near the projected center of the remnant and drops nonmonotonically toward the edge of the remnant. Also, W44 has several bright diffuse regions, but no limb or edge brightening.

W44's spectra reveal emission lines, the handiwork of thermal processes. Least squares

fitting between the previously observed spectra and collisional ionization equilibrium spectral models favored temperatures from ~ 4 to $\sim 10 \times 10^6$ K (Smith et al. 1985; Jones, Smith, & Angellini 1993; Rho et al. 1994; Harrus et al. 1996). Fits to the *ROSAT* spectra for various regions showed that the best-fit temperature varies little across the remnant (Rho et al. 1994). Furthermore, the plasma within the remnant's central region appears to be near collisional ionization equilibrium; the ionization timescale of $2.0^{+4.3}_{-0.7} \times 10^{11}$ s cm^{-3} and the temperature of $\sim 1.02 \pm 0.16 \times 10^7$ K, found from the combined *ROSAT*, *Einstein*, and *Ginga* data (Harrus et al. 1997) place the plasma near the collisional ionization equilibrium state on Vedder et al. (1986)'s plot. Other centrally bright remnants also exhibit small temperature gradients and are near collisional ionization equilibrium (or, as in the case of IC443 (Kawasaki, et al. 2002), overionized). The most relevant properties derived from the observations of W44 are tabulated in Table 1.

Table 1.

Physical Characteristic	Previous Observational Support
Age of $\sim$20,000 yr	Pulsar timing observations
Thermal X-ray Bright Center, no X-ray shell	*EXOSAT, ROSAT, ASCA*
$\sim$ Isothermal X-ray Emission, $T \sim 4$ to 10×10^6 K	*EXOSAT, ROSAT, ASCA*
Partially formed cool shell	Radio continuum, H I, [S II], Hα
Density enhancements in shell	OH masers, [O I]

3. Suggested Explanations for W44's X-ray Characteristics

Early researchers demonstrated that the observations are inconsistent with the Sedov-Taylor model, the "standard model", in which the SNR is in the adiabatic phase of development, and evolves in a homogeneous media without thermal conduction, turbulent mixing, or evaporating clouds. For example, the observations reveal no X-ray edge brightening, while the adiabatic phase models predict a very bright edge. The observations reveal an X-ray bright projected center, while the adiabatic phase models predict the center to be the dimmest region. Also, the observations reveal near isothermality within the remnant, while the adiabatic phase models predict strong temperature gradients. To explain W44's very bright center, dim edge, and near isothermality, several scenarios have been proposed, each with implications for the evolution of supernova remnants and the physics of the interstellar medium.

3.1. Obscuration and Shell Formation

Because W44 is heavily obscured, the earliest explanation for the lack of observed X-ray edge brightening was that the lower energy X-rays from the anticipated edge were preferentially absorbed by the intervening material. Long, et al. (1991) used Sedov models to rule out this explanation for W28 and 3C400.2. Subsequently, Shelton et al. (1995), Harrus et al. (1997), and Shelton et al. (1999) used hydrodynamic codes to show that the lack of a bright edge for W44 was more likely to be because the remnant had evolved beyond the adiabatic phase and into the radiative phase in which the periphery has cooled (also see Cox et al. (1999)). This interpretation is consistent with the radio continuum evidence for shell formation and has been suggested for other centrally bright remnants as well (i.e. 3C 397 (Safi-Harb et al. 2000), 3C391 (Chen & Slane 2001), IC443 (Kawasaki, et al. 2002), N206 in the Large Magellanic Cloud (Williams et al. 1999), and 0045-734 and 0057-7226 in the Small Magellanic Cloud (Yokogawa et al. 2002)) While this evolutionary explanation could easily explain why thermal composite remnants lack X-ray bright shells, it does not additionally explain the bright emission from the center. That phenomena prompted the following theories.

3.2. Evaporating Cloudlets

Considering that the interstellar medium is inhomogeneous, White & Long (1991) suggested that supernova shock fronts might sweep past cloudlets. If the cloudlets evaporate

within a particular range of timescales (similar to or longer than the age of the SNR, but not long enough to provide significant evaporated mass), then they could load the remnant interiors with material. The advantages of this model are that the entrained material could both increase the center's luminosity and dampen the temperature gradient. This model may also explain Hα, [OI], and OH maser observations (see Chevalier (1999) for astrophysical analysis and observational review). The disadvantages are that cloudlets have difficulty passing through the shock front intact (Stone & Norman 1992), cloudlet evaporation requires the unlikely phenomenon of thermal conduction through a sheath of dense and tangled magnetic fields lines, the predicted remnant ages do not agree with other estimates (compare ages calculated by Rho et al. (1994) and Harrus et al. (1997) with Wolszczan, Cordes & Dewey (1991)'s estimate for W44 or the inconsistency in MSH 11-61A's age estimates (Jones, et al. 1998)), and detailed calculations do not predict the observed sharp X-ray surface brightness gradient in the center (compare Figure 3 of Harrus et al. (1997) with Figure 13 of Shelton et al. (1999)). Although no detailed hydrodynamic and spectral simulations of supernova remnants with evaporating clouds have been published, we can sketch the broad outlines of such spectra from the characteristics of the evaporating cloud model. Such spectra should have an evaporating cloud component and a supernova remnant component. The evaporating cloud model claims that the majority of the flux from the central section of the remnant is due to evaporating clouds, while the minority of the flux derives from the supernova remnant itself. The most recent evaporate should be very underionized material embedded in a matrix of hotter gas, although the older material would have had more time to approach equilibrium with the hot matrix. Later in the paper, we will examine the *Chandra* spectra for such features (see Section 4.3).

3.3. Entropy Mixing (such as Thermal Conduction or Bulk Motion)

Thermal conduction or turbulent mixing (even if only operational during the remnant's early evolution) could redistribute entropy throughout the remnant's interior. As a result, the interior could be made roughly isothermal, isobaric, and isochoric (see calculations in Cox et al. (1999) and hydrodynamic simulations in Shelton et al. (1999)). In this scenario, the remnant's interior, and especially its center, would be denser than a non-conductive or unmixed SNR. Because of its comparatively larger interior density and more moderate temperature, the entropy-mixed SNR would have a bright interior. Thus, the advantages of this model are that it predicts a luminous center and small temperature gradient. The disadvantage is that it may require thermal conduction in the presence of some magnetic fields, though in a far more likely manner than thermal conduction across the tangled magnetic fields surrounding the putative embedded clouds. Further, as with the evaporating cloud

model, the detailed calculations do not predict the sharp X-ray surface brightness gradient observed near W44's projected center (see Figure 13 of Shelton et al. (1999)) Note that two dimensional models of thermally conductive remnants appear to require longer evolutionary times or larger ambient densities in order for the remnant to evolve into the radiative phase (compare 2-d models in Shelton et al. (1999) and Velázquez et al. (2003) with 1-d models in Shelton et al. (1999)). The spectra of an entropy-mixed SNR should have a small temperature gradient with respect to radius. With the exception of dust destruction effects, the plasma should be nearing ionization equilibrium and may even be recombining. This model will be tested by comparing the *Chandra* spectra with detailed hydrodynamic and spectral simulations in Section 4.3.

3.4. Metal Enrichment Gradients

Supernova explosions eject a few solar masses of metals into the supernova remnant. For example, Thielemann et al. (1996) predict yields of 0.03 to 0.6 $M_\odot$ of neon, 0.012 to 0.2 $M_\odot$ of magnesium, 0.05 to 0.12 $M_\odot$ of silicon, 0.02 to 0.04 $M_\odot$ of sulfur, and 0.06 to 0.15 $M_\odot$ of iron for 13 to 25 $M_\odot$ progenitor stars. If the yields were spread evenly throughout the remnant, then they would make insignificant contributions to the total metallicity of the plasma. But, the material in a remnant of W44's age is not completely mixed from center to edge. The ejecta should preferentially enrich the remnant's center at the expense of the remnant's periphery which predominately consists of swept up interstellar matter. Considering that the details of the mixing are not currently known, let us suppose, that the ejecta are mixed over one half of the remnant's radius. Let us also suppose that the volume density in the center of the remnant is about one tenth that of the ambient medium, as is found for thermally conductive remnants entering the radiative phase of evolution (Cox et al. 1999). If, in contrast, the entropy is not mixed, then the central volume density would be much less and the argument would become much stronger. Assuming that the remnant is approximately 19pc $\times$ 16.5pc $\times$ 23pc, the pre-explosion volume density was roughly 6 atoms cm^{-3} (Cox et al. 1999; Shelton et al. 1999), and the plasma has Anders & Grevesse (1989) metal abundances, then the central eighth of the remnant's volume should contain 0.03 $M_\odot$ of neon, 0.01 $M_\odot$ of magnesium, 0.01 $M_\odot$ of silicon, 0.006 $M_\odot$ of sulfur, and 0.03 $M_\odot$ of iron due to the swept up interstellar matter. Therefore the swept up ISM's contribution to the number of metal atoms in the central portion of the remnant is smaller than the ejecta's contribution and therefore the swept up ISM metals should not obscure a gradient in the ejecta's spatial distribution.

Another source of a metallicity gradient is dust destruction within the remnant. Dust in

pre-shock ISM typically depletes 95% of the magnesium and silicon, 50% of the sulfur, and 98% of the iron, but none of the neon from the gas phase (Vancura et al. 1994). These atoms will rejoin the gas phase as the dust is destroyed. In time, they would experience collisions, raising their temperature and ionization state. We anticipate that the spatial pattern of metal re-injection is a complex result of multiple process. On one hand, the material in the remnant's center has experienced the strongest shocks and the greatest lengths of time at the highest temperatures. These factors favor dust destruction (Tielens et al. 1994) in the remnant's center. On the other hand, dust destruction behind non-radiative shocks (earlier in the remnant's history) is a strong function of the volume density and therefore of the swept up post-shock column density (Vancura et al. 1994). Considering that the zone of swept up material behind the shock front grows in column density as a remnant ages, the outermost parts of W44 would be favored regions for dust destruction.

A metallicity gradient, whether from dust destruction or ejecta, would result in a gradient in the specific luminosity, which would contribute to the observed surface brightness gradient. Such an argument has previously been made in other papers, including Shelton et al. (1999), and Yokogawa et al. (2002). Elevated abundances have already been observed in a few older remnants, including both centrally peaked type remnants (Yokogawa et al. (2002) for the total spectra of two centrally peaked SMC remnants) and edge brightened remnants (Miyata & Tsunemi (1999) for the interior of the Cygnus Loop). In the past, it was not possible to test W44 for radial abundance trends because the previous observations lacked sufficient spatial resolution. Now, abundance gradient measurements are viable using the *Chandra* data and may be of use in explaining W44's morphology as well as constraining future mixing and dust destruction calculations. We will report on the results in Sections 4.2 and 4.3.

3.5. Density Gradients

Recently, Petruk (2001) pointed out that if the ambient medium has a large scale density gradient, then the shells of adiabatic-phase remnants will have non-uniform X-ray surface brightness. The portion of the shell at the denser end can produce more X-rays than the portion of the shell on the more diffuse end. If the remnant is viewed along the direction of the density gradient, then its projected center can appear to be brighter than its extremities. Note that in this model, the X-ray bright shell at the periphery of the projected remnant would also be somewhat bright. Analyses of previous X-ray data did not find such an X-ray bright shell (Rho et al. (1994), Harrus et al. (1997), Shelton et al. (1999)). The *Chandra* data has finer spatial resolution and we will use it for a refined search for an X-ray shell (see

Section 4.1).

4. *Chandra* Observations and Analysis

W44 was observed by *Chandra* for 46 ksec on October 31, 2000. Six ACIS chips (ACIS-S chips 1 through 5 and ACIS-I chip 3) were active during the observation. The data were calibrated using caldb 2.2.1. Since CTI correction using the software of (Townsley et al. 2000) was only available for two of the five ACIS-S chips, and applying CTI corrections to the S3 data did not change spectra fit parameters, we did not apply the CIT corrections in order to retain chip-to-chip consistency over all of the chips in use. Periods containing soft background flares (Markevitch 2001a) were determined from the light curve and removed. Point sources were detected using the CIAO *wavedetect* algorithm. The S4 chip was de-striped using the algorithm developed by Houck (2000) as this analysis was done before the destreak task was implemented in CIAO. The redistribution matrix files (RMFs) and auxillary response files (ARFs) for extended regions were calculated using the CIAO *mkwarf* and *mkrmf* tasks.

Our determination of the instrumental and cosmic background began with the front-illuminated chip I3 and the back-illuminated chip S1, which sampled off-remnant portions of the sky and have measured instrumental backgrounds. The instrumental background can be extracted from observations of the dark moon or calculated from event histogram data. In either case, the measured instrumental background must be scaled to the strength of the background during the observation using the $10.5 - 12.9$ keV range where the *Chandra* response is minimal. However, as we found significant differences in the shape in that spectral range between our data and the event histogram data then extant, but found that the dark moon data matched the W44 data quite well, we used the dark moon data for the spectral shape of the instrumental background.

The cosmic background in the direction of W44 consists of very soft foreground emission due to the Local Hot Bubble and absorbed background emission from the hard Galactic ridge. The cosmic background was determined from a spectrum derived from the off-SNR region of chip I3, after scaling and removal of the instrumental background. Chip I3's combined cosmic and instrumental background compares well with that of chip S5, the only other front-illuminated chip having some exposure to the off-SNR sky. Given the differences in responses among the chips, we did not directly subtract the chip I3 background from other spectra. Instead, we fit a reasonable thermal model to the chip I3, cosmic background, and then used that model, scaled by the solid angle covered, to remove the cosmic background from chips entirely covered by the SNR. To this model was added a powerlaw (which was

not convolved with the response function) in order to model the contribution from low-level background flares to the instrumental backgrounds on the BI chips.

Chips S2, S3, and S4 viewed the center and interior of the remnant, without viewing off-SNR regions. We constructed a background spectrum for chips S2 and S4 from the cosmic background spectrum determined from the chip I3 off-SNR observations and the instrumental background spectrum determined from the chip S2 observations of the dark moon. We constructed a background spectrum for chip S3, a back-illuminated chip, determined the cosmic background spectrum from the cosmic background spectrum determined from the chip I3 off-SNR observations and the instrumental background spectrum determined from the chip S3 observations of the dark moon. In general, the cosmic background is poorly characterized, primarily due to the low count rates, but this is not a significant problem. Figure 2 shows that the contribution by the cosmic background spectrum is comparable to that of the instrumental background for the 0.5-2.0 keV energy interval and is small compared to the strength of the W44 spectrum on the S2-S4 chips in the spectral region of interest.

4.1. Images

The ACIS-S chips were "laid along" the long axis of the supernova remnant, such that Chips S2, S3, and S4 viewed the center of the remnant, while chips S1 and S5 viewed the southeast and northwest edges of the remnant and the adjacent sky. The pulsar synchrotron nebula lies near the center of the remnant (Wolszczan, Cordes & Dewey 1991) and so was positioned on chip S2. The *Chandra* observations of the pulsar wind nebula are analyzed in a separate paper (Petre et al. 2002). Although the pulsar and its wind nebula emit sufficient numbers of X-ray photons to be significantly detected during the *Chandra* observation, the pulsar and nebular photons do not hinder the observation of the W44 supernova remnant. The ACIS I3 chip viewed the western edge of the remnant. Figure 1 shows the positioning of the ACIS chips with respect to the radio image. These X-ray images were smoothed with a 11.8 arcsec HWHM Gaussian.

The *Chandra* data beautifully and clearly show that the emissive region extends to the periphery of the remnant, but that the radio outline and the X-ray outline may not be identical. The X-ray emissive region may extend slightly beyond the radio synchrotron emissive region in the northwest and vice-verse in the southwest. Both the radio and X-ray surface brightnesses fade gradually near the periphery, so the apparent discrepancy could be due to differences in emissivities and observational sensitivities. As in previous X-ray observations of W44, no X-ray bright shell is discernible in the images. The greatest

surface brightnesses near the remnant's edge on Chips S1, S5, and I3 are 2×10^{-4} counts s^{-1} arcsec^{-2}, 4.5×10^{-4} counts s^{-1} arcsec^{-2}, and 2×10^{-4} counts s^{-1} arcsec^{-2}. The corresponding background rates are 8×10^{-5} counts s^{-1} arcsec^{-2} for Chip S1, 6×10^{-5} counts s^{-1} arcsec^{-2} for Chip S5, and 6×10^{-5} counts s^{-1} arcsec^{-2} for Chip I3. The average intensity of the central 20 arcmin of the remnant is two to three times stronger than that of the outer 10 arcmin of the remnant. Much of the emission in the central 20 arcmin originates in several bright regions strung along the long axis of the remnant.

4.2. Spectra

As an introduction, we present the integrated spectra from individual chips before discussing the spectra taken from smaller regions of the chips. The prominent lines and complexes in the ACIS chip S2, S3, and S4 spectra (see Figure 3) are Ne IX ($\sim$ 910 eV), Ne X (1010 eV), Mg XI ($\sim$ 1340 eV), Mg XII (1450 eV), Si XIII ($\sim$1850 eV), Si XIV (1980 eV), and S XV ($\sim$2450 eV). The prominant emission lines of Ne IX, Ne X, Mg XI, Mg XII, Si XIII, Si XIV, and S XV are expected to be strong in $\sim 10^{6.6}$-$10^{7.2}$ K plasma (Raymond & Smith 1977), if the plasma is assumed to be in collisional ionizational equilibrium plasma (we will discuss non-equilibrium models later). The higher energy features are expected to be stronger in $\sim 10^{7.2}$ K gas, while the lower energy features are expected to be stronger in $\sim 10^{6.6}$ to $10^{7.0}$ K gas (Raymond & Smith 1977). The spectrum of the central region of the remnant (chip S3) is harder and more influenced by $\sim$1850 eV (Si XIII) and $\sim$ 2450 eV (S XV) emission lines than the spectra from the surrounding regions (chips S2 and S4). The contrast suggests that the center is a few times hotter than the adjacent regions.

The X-ray emission detected by chips S2, S3, and S4 lacks the Fe XVII spectral feature at 1120 eV. As a result, we expect little emission in the Fe XVII feature at 1020 eV and attribute the observed $\sim$ 1000 eV feature solely to Ne X (1010 eV). The dearth of very highly ionized iron is corroborated by the following spectral modeling as well as that of the *ASCA* data (Harrus et al. 1997). When the Fe abundance is allowed to vary in the "VNEI" model (variable abundance non equilibrium ionization spectral model using Mazzotta et al. (1998)'s ionization fractions) in the XSPEC spectral fitting software, the model which best fits the chip S3 spectrum between photon energies of 0.35 and 8.00 keV has an Fe abundance relative to the other elements of 0.04 ± 0.01. In this model, the temperature (T) is $9.8 \pm 0.1 \times 10^6$ K, the ionization timescale (τ) is $2.0^{+\infty}_{-1.7} \times 10^{13}$ s cm^{-3} (hence the plasma is near ionization equilibrium), and the absorbing column density (N_H) is $9.2 \pm 0.1 \times 10^{21}$ cm^{-2}. The reduced chi-square parameter (χ^2_ν) is 5.0. Figure 4 displays this spectral model and the S3 data, while Table 4.2 reiterates the model parameters. Although the model spectrum fits the

gross features of the spectrum, it overpredicts some feature intensities while underpredicting others, such as the ∼850 eV bump. Because the strength of any given feature depends on the plasma's temperature and extent of ionization, models composed of two spectra provide a better match to the assorted features of this spectrum. One reason why such models are physically understandable is because the line of sight intersects differing parts of the remnant and possibly plasmas of differing qualities. The best fitting two component model is presented in Table 4.2. As is shown in Figure 4, this model fills in the ∼850 eV bump with emission from an iron rich, poorly ionized, hot plasma. It is also possible to fill in the bump with emission from an iron rich, poorly ionized, plasma of lower temperature (see Table 4.2). The common and important aspect of the second component is that it contains poorly ionized iron. In both cases, the second component provides only $\sim 10\%$ of the flux of 0.35 to 8.00 keV photons. This component can be explained if much of the iron had been locked in dust grains when the supernova shock swept through the plasma. If the iron was released from the grains as or after the plasma was shock heated, then its ionization would lag that of other elements. Note that the chip S3 data and, to a lesser extent, the S2 and S4 data exhibited a slight energy shift. The relative shift between S3 and S2/S4 spectra has been seen in other data sets, reported to the Chandra Science Center, and removed using the fitting software; the shift in S2/S4 may be due to the long-term gain drift for which this data had not been corrected.

In comparison to the central region, the single temperature, non equilibrium fits to the neighboring regions (chips S2 and S4) prefer somewhat lower temperatures, $6.9 \pm 0.1 \times 10^6$ K and $7.0 \pm 0.1 \times 10^6$ K, respectively. The ionization timescales for these models are $9.3^{+\infty}_{-5.5} \times 10^{12}$ s cm^{-3} and $2.8^{+\infty}_{-1.4} \times 10^{13}$ s cm^{-3}, respectively (indicating, again, that the plasma is near collisional ionizational equilibrium), the relative Fe abundances are 0.37 ± 0.02 and 0.50 ± 0.02, respectively, and the absorbing column densities are $1.2 \pm 0.1 \times 10^{22}$ cm^{-2} and $1.4 \pm 0.1 \times 10^{22}$ cm^{-2}, respectively. The reduced chi-square parameters are 5.2 and 4.1, respectively. Two temperature fits were also performed. These model parameters are presented in Table 4.2. In accord with the results of the *ROSAT* data analysis (Rho et al. 1994; Shelton et al. 1999), we find that the temperature profile is far too flat to be consistent with Sedov model predictions.

Chip	Spectral Model	T (10^6 K)	τ (s cm^{-3})	Relative **Iron** Abundance	N_H (cm^{-2})	χ^2_ν
S3	vnei	9.8 ± 0.1	$2.0^{+\infty}_{-1.7} \times 10^{13}$	0.04 ± 0.01	$9.2 \pm 0.1 \times 10^{21}$	5.0
”	2 temp vnei	8.8 ± 0.1	$2.0^{+\infty}_{-1.7} \times 10^{13}$	0.07 ± 0.01	$1.2 \pm 0.1 \times 10^{22}$	2.7
	and	49.0 ± 2.7	$4.6 \pm 0.1 \times 10^{9}$	6.51 ± 0.66	”	
”	2 temp vnei	9.1 ± 0.1	$2.0^{+\infty}_{-1.7} \times 10^{13}$	0.08 ± 0.12	$1.3 \pm 0.1 \times 10^{22}$	3.6
	and	7.7 ± 0.5	$1.4 \pm 0.1 \times 10^{10}$	2.43 ± 0.32	”	
S2	vnei	6.9 ± 0.1	$9.3^{+\infty}_{-5.5} \times 10^{12}$	0.37 ± 0.02	$1.2 \pm 0.1 \times 10^{22}$	5.2
”	2 temp vnei	3.5 ± 0.1	$3.6^{+\infty}_{-0.1} \times 10^{13}$	0.58 ± 0.04	$1.6 \pm 0.1 \times 10^{22}$	2.5
	and	12.5 ± 0.2	$1.6^{+\infty}_{-1.3} \times 10^{13}$	0.00 ± 0.11	”	
S4	vnei	7.0 ± 0.1	$2.8^{+\infty}_{-1.4} \times 10^{13}$	0.50 ± 0.02	$1.4 \pm 0.1 \times 10^{22}$	4.1
”	2 temp vnei	3.3 ± 0.1	$6.5^{+\infty}_{-3.1} \times 10^{12}$	0.83 ± 0.06	$1.7 \pm 0.1 \times 10^{22}$	2.2
	and	10.4 ± 0.2	$3.0^{+\infty}_{-2.7} \times 10^{13}$	0.24 ± 0.06	”	

In order to examine the spectral trends on finer angular scales, we subdivided the central third of the ACIS S field of view into 30 segments along the long axis of the remnant (see Figure 5). We then compared the spectra with spectral models. Because the previous analysis found most of the emission to be from nearly equilibrium plasma, equilibrium models were used. The temperatures found by fitting the segments' spectra with single temperature, equilibrium, variable abundance spectral models (the VMEKAL model on XSPEC (Mewe, Lemen, & van den Oord 1986; Kaastra 1992; Liedahl, Osterheld, & Goldstein 1995), with Ne, Mg, S, Si, and Fe abundances allowed to vary) are plotted in Figure 6. Figure 6 also displays the reduced χ^2 for the fits. Again, the temperature profile is flatter than predicted by the Sedov model.

As Figure 7 illustrates, the abundances of neon, silicon, sulfur, and iron peak near the remnant's projected center. The most logical sources of these abundance gradients are the ejecta distribution and more advanced dust destruction in the remnant's center. We suspect that both phenomena are operating for the following reasons. Because neon, an inert element, cannot be easily bound into dust, the neon abundance gradient cannot be attributed to dust destruction. Therefore, the existence of a gradient in the neon distribution indicates the presence of ejecta. The iron abundance distribution suggests that dust destruction is also occuring. The iron-rich component in the two component fits to the S3 full-chip data indicates that the iron atoms are less ionized than the other elements. The paucity of equilibrium ionization iron and the presence of underionized iron could be explained if iron atoms had been released from dust grains during the remnant's lifetime. The elevated abundances near the remnant's projected center would contribute to this region's elevated surface brightness. The 800 to 900 eV feature in chip S3's spectrum appears in the spectra for the outer 2/3 of the chip S3 segments (see Figure 8) and some parts of the flanking chips, but is inconspicuous in the spectra of the remnant's projected center. Presumably, this feature arises from L-shell iron in less ionized gas. As was the case for the chip S3 spectral fitting, this feature cannot be fit by equilibrium spectral models for a wide range in temperatures without overpredicting other emission features, but can be fit by an additional, iron-rich, underionized spectral component.

The bright 'knots' (diameter ~ 1 to 4 arcsec, brightness increase $\gtrsim 1 \times 10^4$ counts cm^{-2} s-1 on chip S4) in the central $\sim$20 arcmin of the remnant have long intrigued researchers. However, before the *Chandra* era, no X-ray telescopes had the sensitivity, spatial and spectral resolution necessary to isolate and study the knots. Figures 1 and 5 show that *Chandra* has successfully resolved the knots; thus the knots do not appear to be composed of smaller substructures (down to the resolution limit of the telescope). Here, we search for spectral differences between the knot emission and the inter-knot emission in the chip S4 data. We are focussing our efforts on the chip S4 data, because these data allow us to distinguish

between radial variation and knot versus interknot variation. For the analysis, chip S4's area was segmented, based on brightness, into 10 regions. These regions have less than 1.34, 1.68, 2.12, 2.42, 2.75, 3.15, 3.56, 3.89, and 4.36 or greater than 4.36×10^{-4} counts cm^{-2} s^{-1}, respectively, in the 0.7 to 3.0 keV energy range. Each has $\sim$8800 counts in this range. The regions are outlined in Figure 9. The spectrum from each of the regions was then fit with variable abundance, non equilibrium spectral models (VNEI, with Ne, Mg, S, Si, and Fe allowed to vary), as well as variable abundance, equilibrium spectral models (VMEKAL, with Ne, Mg, S, Si, and Fe allowed to vary). The ionization parameter in the VNEI fits hovers around 2×10^{13} s cm^{-3}, indicating that the gas is near collisional ionizational equilibrium. Independent of fitting method, we found little trend in temperature (see Figures 10a and b) We did, however, find a trend in the best fit elemental abundances. Figures 10a and b show that the best fitting models for the brighter regions have greater neon, silicon, sulfur, and iron abundances than the best fitting models of the dimmer parts of the chip, though the trend is not uniform. The most obvious interpretations of these fitting results are that more metals have been released from dust and pockets of ejecta in the bright knots than in the dimmer regions. Because increasing the Ne, Mg, S, Si, and Fe abundances results in larger emitted fluxes of 0.7 to 3.0 keV photons, the abundance gradient contributes to the observed surface brightness variation. However, it does not entirely explain the observed surface brightness variation. If the dimmer plasmas observed with parts of chip S4 were to have the Ne, Mg, S, Si, and Fe abundances of the brighter plasmas observed on other parts of chip S4, they would still be dimmer.

4.3. Comparisons with SNR Models

In this section, we compare the *Chandra* data with models of W44. Section 3 lists several suggested explanations for W44's X-ray morphology (obscuration, shell formation, evaporating clouds, entropy mixing, metal enrichment, and density gradients). As stated in Section 3, the first and last explanations are ruled out by observations and/or modeling. The second explanation is well supported, but cannot fully explain W44's X-ray morphology. Therefore, we assume that the remnant has evolved into the shell formation stage while examining the entropy mixing (see Cox et al. (1999), Shelton et al. (1999), or Section 3.3), evaporating clouds (see White & Long (1991), Long, et al. (1991), or Section 3.2) and metal enrichment (Shelton et al. (1999), or see Section 3.4) explanations.

To create our model of the entropy mixed (thermally conductive or turbulently mixed) supernova remnant, we used a detailed hydrodynamic computer simulation. The simulation employs saturated thermal conduction, non-ionizational equilibrium cooling, ionization, and

recombination rates, and magnetic tension and is described in Shelton (1998). The ambient density (6.2 atoms cm^{-3}), explosion energy (1.0×10^{51} ergs), effective magnetic field strength (2.1μG), age (20,000 yrs), and solar metallicities (Anders & Grevesse 1989) are equal to those used in the Cox et al. (1999) and Shelton et al. (1999) articles on W44 simulations. This model meets the observational constraints on age, radius, and degree of H I shell formation. Spectral predictions of this model (though not this particular computer simulation) were compared with previous observations in Shelton et al. (1999). Their thermally conductive simulated remnant was centrally peaked in X-ray emission, significantly more so than the otherwise equivalent nonconductive simulated remnant but, still less than the observed morphology (see Section 3.3 and Figure 13 of Shelton et al. (1999)). Furthermore, their spectral results for the supernova remnant satisfactorarily matched W44's *ROSAT* and *Einstein* data. The χ^2_ν for the combined fit was 2.0. For the *ROSAT* comparison, the spectrum of the entire remnant was used; for the *Einstein* comparison, the spectrum of the central 6' (in diameter) was used.

The source of W44's controversy is its bright projected center, whose photons were easily outnumbered by photons from other parts of the remnant in the *ROSAT* analysis. With *Chandra* data, it is now possible to compare the spectrum of the remnant's center with those of simulated models. The best fit between the central region (using the eighth rectangular segment from the left in Figure 5, though nearby regions gave similar results) and the simulated 0.7 to 2.2 keV spectrum has a reduced χ^2 of 1.5 and is displayed in Figure 12. In the fitting process, the column density of absorbing material is allowed to vary. The best fit case has a column density of $2.1 \pm 0.1 \times 10^{22}$ cm^{-2}.

We also performed a simulation without thermal conduction. The resulting model, with its hot ($\sim 6 \times 10^8$ K), but dim center (as in Figures 11 and 13 of Shelton et al. (1999)), underpredicts the ~ 1.4 and ~ 1.9 keV features of the observed spectrum (see Figure 12). As a result, the reduced χ^2 for the fit is 5.1.

The evaporating clouds scenario was explored by White & Long (1991) and Long, et al. (1991), who predicted the X-ray surface brightnesses as a function of radius, but did not predict the spectra. We cannot adequately predict the spectrum of a supernova remnant containing evaporating clouds without extensively modifying and testing our supernova remnant simulation package. If we were to approximate the evaporating clouds spectrum using a non equilibrium, variable iron abundance spectrum and were to add it to the above non thermally conducting SNR simulation to yield a spectrum for comparison with the observations, we would only be able to constrain the clouds model by its need to bolster the weak ~ 1.4 and ~ 1.9 keV features in the non thermally conducting SNR spectrum. Such a task is achievable, but of limited value. For the interested reader, the parameters of a successful

model are: $T = 6.0 \times 10^8$ K (set), $\tau = 1.7 \times 10^{10}$ s cm^{-3}, relative Fe abundance = 0.32, $N_H = 0.97 \times 10^{22}$ cm^{-2}, and $\chi^2_\nu = 2.1$. In this case, the evaporating clouds produce 70% of the 0.7 to 2.2 keV flux, while the non thermally conductive SNR produces the remaining 30%. The spectrum is displayed in Figure 12. Other combined models, with set temperatures as low as 1×10^8 K were tried and found to succeed similarly well. Although the goodness of these fits appear to add credence to these models, the extreme level of approximation used and the lack of physical tests (such as age, radial surface brightness profile, etc.) are serious detractors.

Earlier, we found a metallicity gradient across the remnant as well as a metallicity gradient associated with knot brightness. Given that a plasma's specific luminosity is an increasing function of its metallicity, these gradients may be contributing to the observed brightness variation. In order to estimate the extent of the contribution to the radial surface brightness gradient, we compared surface brightness profiles found with and without a metallicity gradient. The solid histogram in Figure 13 traces the surface brightness profile of a model plasma having W44's metallicity gradient (for Ne, Mg, S, Si, and Fe), while the dashed histogram traces the surface brightness profile of a model plasma having constant abundances of these elements (equal to the averages of those observed for segments 7_1 through 7_14, an ∼3 arcminute swath). Both models have identical densities, temperatures, and normalizations as a function of off-axis angle. These parameters were found by fitting VMEKAL models to the observations. Figure 13 demonstrates that the abundance gradient contributes substantially to the observed surface brightness gradient. However, it does not explain all of the central brightness. If the abundances had been constant (as in the dashed histogram), the SNR would have exhibited a somewhat centrally enhanced X-ray morphology, similar to that predicted with the entropy mixed SNR simulation and some of those predicted with evaporating clouds calculations.

5. Summary

The *Chandra* image of W44 reveals that the X-ray luminous region extends to the periphery of the remnant outlined in radio observations. These data, like the *ROSAT* data, show that there is no X-ray shell and that the center's surface brightness is as much as several times stronger than that nearer to the periphery. The enhancement can be described as a surface brightness plateau combined with several bright knots within the remnant's central ∼10 arcminutes.

The remnant exhibits a roughly monotonic, but weak spectral gradient, such that the hardest spectra originate near the projected center. By fitting model spectra to the data, we

found that between the center and $\sim 8'$ (~ 6 pc) from the center, the plasma's temperature drops by less than a factor of 2 and the elemental abundances drop by a factor of several. The elevated neon abundance suggests that a portion of the observed metal abundance gradient is due to progenitor ejecta. Additional spectral fits indicate that the gas phase iron atoms are less ionized than the gas phase atoms of other elements. This delayed ionization suggests that iron was released from dust after the gas was shock heated, making this the first X-ray evidence for dust destruction within supernova remnants. Several bright knots dot W44's face. The plasma in these knots was found to have a similar temperature and degree of ionization as the plasma in the surrounding regions, but to have significantly greater gas phase abundances. If the knots had been evaporating clouds, we would not have expected their thermal and ionizational properties to match those of the surrounding regions. If the knots are not evaporating clouds, then their astrophysical origins are even more mysterious than previously thought.

W44 is thought to have evolved into the radiative phase, and therefore no longer has a hot, X-ray emitting shell. Acting alone, this effect would leave the remnant's center relatively dim and result in a quasi-edge brightened appearance, not yet consistent with the observations (compare dashed curve with symbols in Figure 13 of Shelton et al. (1999)). Previous papers have shown that obscuration plays a role, but not the one originally assigned to it. Obscuration preferentially diminishes the flux of softer X-rays emitted at the larger radii, but the effect is not strong enough to explain the remnant's centrally brightened appearance.

The unexpectedly bright centers of W44 and similar remnants inspired the White & Long (1991) hypothesis for evaporating clouds within these remnants. W44's bright knots were assumed to be evaporating clouds or associations of evaporating clouds, and so taken as further evidence for cloud evaporation. In the evaporating clouds hypothesis, the material evaporated off of the clouds contributes substantially to the density of hot gas in the remnant's center and boosts the center's X-ray luminosity. But, the predicted radial gradient in surface brightness in the evaporating clouds models for W44 is far flatter than the observed gradient and W44's predicted age is far less than the observationally determined age (see Jones, Smith, & Angellini (1993); Wolszczan, Cordes & Dewey (1991); Harrus et al. (1997); Rho et al. (1994)). Furthermore, we learned from the *Chandra* analysis that the temperature and ionization parameter do not strongly and significantly vary from the knot regions to the interknot regions, suggesting that the knots do not signify cloud evaporate. Alternatively, if the hypothetical evaporating clouds were much smaller then the knots then it would be useful to compare the *Chandra* spectra with a spectral predictions from models. Unfortunately, there are no published spectral predictions for this scenario. We mocked-up spectral models by combining a detailed hydrocode SNR simulation with non-equilibrium models

of hot, recently heated gas (representing the gas evaporated off of clouds). We found the combined models to be good fits to the *Chandra* spectrum ($\chi^2_\nu \cong 2.2$), though the combined models are not particularly physical and the fits are not particularly constraining.

The entropy mixed model was previously shown to predict a bright center, though also with a far smoother radial gradient than observed. The *ROSAT* spectrum for the entire remnant and the *Einstein* spectrum for the central 6' (in diameter) were found to be well matched to the spectra predicted from a detailed hydrocode model which included entropy mixing in the form of thermal conduction (Cox et al. 1999; Shelton et al. 1999). Capitalizing on *Chandra*'s spatial resolution, in this paper we examined the source of the controversy, the remnant's bright center. We compared the spectrum from the remnant's center with detailed hydrocode model predictions, finding them to be a good match ($\chi^2_\nu \cong 1.5$). The balance of evidence favors the entropy mixing model over the cloud evaporation model and over the standard, adiabatic, Sedov-Taylor model ($\chi^2_\nu \cong 5.1$), but none of these models explains **all** of the central flux.

The observed radial gradient in abundances and the correlation between the knots and abundances were new discoveries made possible by the *Chandra* data. The additional metals in the remnant's projected center raise the flux, making the remnant's projected center brighter than outlying areas. The abundance gradient is nearly strong enough to fill the gap in brightness between the observations and either the entropy mixing or the evaporating clouds model.

Acknowledgements:

We acknowledge the financial support from CXC grant GO1-2057A. RLS acknowledges discussions on evaporating cloud models with Knox Long and mixing with Sally Oey. KDK acknowledges discussions on the instrumental background with P. Plucinsky, C. Grant, B. Biller, S. Wolk, K. Arnaud, K. Gendreau, and M. Markevitch.

REFERENCES

Caswell, J. L., Murray, J. D., Roger, R. S., Cole, D. J., & Cooke, D. J. 1975, A&A, 45, 239

Chen, Y. & Slane, P. O. 2001, ApJ, 563, 202

Chevalier, R. A. 1999, ApJ, 511, 798

Claussen, M. J., Frail, D. A., Goss, W. M., & Gaume, R. A. 1997, ApJ, 489, 143

Clemens, D. P. 1985, ApJ, 295, 422

Cox, D. P., Shelton, R. L., Maciejewski, W., Smith, R. K., Plewa, T, Pawl, A., & Rozyczka, M. 1999, ApJ, 524, 179

Dame, T. M., Elmegreen, B. G., Cohen, R. S., & Thaddeus, P. 1986, ApJ, 305, 892

Frail, D. A., Giacani, E. B., Goss, W. M,., & Dubner, G. 1996, ApJ, 464, L165

Frail, D. A., Goss, W. M., Reynoso, E. M., Giacani, E. B., Green, A. J., & Otrupcek 1996, AJ, 111, 1651

Giacani, E. B., Dubner, G. M., Kassim, N. E., Frail, D. A., Goss, W. M., Winkler, P. F., & Williams, B. F. 1997, AJ, 113, 1379

Grevesse, N. & Anders, E. 1989, in AIP Conference Proceedings 183, Cosmic Abundances of Matter, ed. C. J. Waddington, p. 1

Gronenschild, E. H. B. M., Mewe, R., Heise, J., den Boggende, A J. F., Schrijver, J., & Brinkman, A. C. 1978, A & A, 65, 9

Harrus, I. M., Hughes, J. P. and Helfand, D. J. 1996, ApJ, 464, L161

Harrus, I. M., Hughes, J. P., Singh, K. P., Koyama, K., & Asaoka, I. 1997, ApJ, 488, 781

Houck, J. 2000, Chandra Science Center memo

Jones, L. R., Smith, A., & Angellini, L. 1993, MNRAS, 265, 631

Jones, T. W., Rudnick, L., Jun, B.-I., Borkowski, K. J., Dubner, G., Frail, D. A., Kang, H., Kassim, N. E., & McCray, R. 1998, PASP, 110, 125

Kaastra, J.S. 1992, An X-Ray Spectral Code for Optically Thin Plasmas (Internal SRON-Leiden Report, updated version 2.0)

Kassim, N. E. 1992, AJ, 103, 943

Kawasaki, M., Ozaki, M., Nagase, F., Masai, K., Ishida, M., & Petre, R. ApJ, 2002, ApJ, 572, 897

Koo, B.-C., & Heiles, C. 1995, ApJ, 442, 679

Kovalenko, A., V., Pynzar', A. V., & Udal'tsov, V. A. 1994, Astron. Rep., 38, 78

Liedahl, D.A., Osterheld, A.L., and Goldstein, W.H. 1995, ApJL, 438, 115

Long, K. S., Blair, W. P., White, R. L., and Matsui, Y. 1991, ApJ, 373, 567

Markevitch, M. 2001a, http://cxc.harvard.edu/contrib/maxim/bg/index.html

Mazzotta, P., Mazzitelli, G., Colafrancesco, S., & Vittorio, N. 1998, A&AS, 133, 403

Mewe, R., Lemen, J.R., and van den Oord, G.H.J. 1986, A&AS, 65, 511

Miyata, E. & Tsunemi, H. 1999, ApJ, 525, 305

Petre, R., Shelton, R. L. & Kuntz, K. D. 2002, ApJ, 579, 404

Petruk, O. 2001, A & A, 371, 267

Raymond, J. C. & Smith, B. W. 1977, ApJS, 35, 419

Reach, W. T. & Rho, J.-H. 1996, A & A, 315, L277

Rho, J.-H., Petre, R., Schlegel, E., & Hester, J. J. 1994, ApJ, 430, 757

Safi-Harb, S., Petre, R., Arnaud, K. A., Keohane, J. W., Borkowski, K. J., Dyer, K. K., Reynolds, S. P., & Hughes, J. P. 2000, ApJ, 545, 922

Sato, F. 1986, AJ, 91, 378

Shelton, R. L., Smith, R. K., & Cox, D. P. 1995, BAAS, 27(3), 186.5904

Shelton, R. L., Cox, D. P., Maciejewski, W., Smith, R. K., Plewa, T, Pawl, A., & Rozyczka, M. 1999, ApJ, 524, 192

Shelton, R. L. 1998, ApJ, 504, 785

Stone, J. M. & Norman, M. L. 1992, ApJ, 390, L17

Smith, A., Jones, L. R., Watson, M. G., Willingale, R., Wood, N., & Seward, F. D. 1985, MNRAS, 217, 99

Szymkowiak, A. 1980, Type I supernovae; Proceedings of the Texas Workshop, Austin, TX, March 17-19, 1980. (A82-34376 16-90) Austin, TX, University of Texas, 1980, p. 32-41

Thielemann, F.-K., Nomoto, K. & Hashimoto, M.-A. 1996, ApJ, 460, 408

Tielens, A. G. G. M., McKee, C. F., Seab, C. G. & Hollenbach, D. J. 1994, ApJ, 431, 321

Townsley, L. K., Broos, P. S., Garmire, G. P., & Nousek, J. A. ApJ, 2000, 534, L139

Vancura, O., Raymond, J. C., Dwek, E., Blair, W. P., Long, K. S. & Foster, S. 1994, ApJ, 431, 188

Vedder, P. W., Canizares, C. R., Markert, T. H., & Pradhan, A. K. 1986, ApJ, 307, 269

Velázquez, P. F., Martinell, J., & Raga, A. C. 2003, Rev Mex A A, 15, 246

Westerhout, G. 1958, BAN, 14, 215

White, R. L. & Long, K. S. 1991, ApJ, 373, 543

Williams, R. M., Chu, Y.-H., Dickel, J. R., Petre, R., Smith, R. C., Tavarez, M. 1999, ApJS, 123, 467

Wolszczan, A, Cordes, J. M., & Dewey, R. J. 1991, ApJ, 372, L99

Yokogawa, J., Imanishi, K., Koyama, K., Nishiuchi, M., & Mizuno, N. 2002, PASJ, 54, 53

This preprint was prepared with the AAS LaTeX macros v5.2.

Fig. 1.— The *Chandra* image (color) overlayed on the radio frequency map (contours) of W44. For the *Chandra* image, the energy bandwidth is 700 to 2600 eV and the smoothing HWHM is 11.8 arcsec. For the radio map, the wavelength is 20 cm and the beamsize is 15.8×15.4 arcsec^2. The radio map is from Frail et al. (1996a).

Fig. 2.— *Top:* Comparison of the W44 spectra from chips S2 and S4 with the instrumental background and the sum of the instrumental and cosmic backgrounds. The instrumental background (labelled "Dark Moon on S2") is that for chip S2 derived from the dark moon data, while the cosmic background spectrum (labelled "Obs. Fore/Back on I3") was derived from chip I3. *Bottom:* W44's spectrum and the instrumental background on chip S3.

Fig. 3.— Spectra extracted from ACIS S2, S3, and S4 data. Left Panel: Spectrum of the projected center of the remnant, taken with the S3 chip. Right Panel: Spectra of the projected off-center interior, taken with the S2 (solid curve) and S4 (dotted curve) chips. In each plot, the low surface brightness curve is the particle background. The particle background bump coinciding with the Si XIII feature in the chip S3 spectrum is associated with Al Kα.

Fig. 4.— Left Panel: Data from the S3 chip (crosses) and best fit single temperature non equilibrium model with variable Fe abundance (solid histogram). The model fits the gross features of the spectrum, but underpredicts the $\sim$ 850, $\sim$1350 (Mg XI) and $\sim$1850 eV (Si XIII) features and overpredicts the $\sim$1450 eV (Mg XII) feature. Right Panel: Data from the S3 chip (crosses) and best fit two component non equilibrium model with variable abundances of iron (solid histogram). This model better predicts the $\sim$ 850 eV, $\sim$ 1450 eV, and $\sim$ 1850 eV features at the expense of underpredicting the $\sim$ 1000 eV feature. The parameters of these models can be found in the text and Table 4.2.

Fig. 5.— The long axis of the remnant has been segmented into 30 regions, which are outlined in this 700 to 2600 eV image and used in subsequent analyses.

Fig. 6.— Plots of estimated plasma temperature and reduced χ^2 as a function of angle from the center of the remnant (center of chip S3). Angles increase to the northwest and decrease to the southwest. Each plasma temperature estimate and reduced χ^2 value corresponds to the best fitting MEKAL spectral model for the spectrum extracted from the appropriate region of the Chandra data. The region widths vary. The symbols are placed at the centers of the regions.

Fig. 7.— Plots of estimated abundances relative to solar as a function of angle from the center of the remnant (center of chip S3). The first, second, third, and fourth panels, respectively, display the neon, silicon, sulfur, and iron abundances relative to solar found from VMEKAL

fits to the data.

Fig. 8.— Spectra from every third segment on the S3 chip. The region numbering begins with "region 7,0", the most southeastern region and terminates with "region 7,15", the most northwestern region. The observed spectra are noted with crosses. The overlayed curves, noted by solid histograms, are the best fit depleted iron MEKAL equilibrium model spectra. Below each spectrum lies a linear plot of the residuals. The ordinate range on the residual plots is -0.04 to 0.04 counts cm^{-2} s^{-1} keV^{-1}. The ~ 850 eV features, which are more obvious in the off-center spectra, are difficult to fit with equilibrium models.

Fig. 9.— The Chip S4 area was segmented based on a brightness criterion.

Fig. 10.— Plot of model parameters versus region number for the VNEI fits to the flux-selected regions on chip S4. (Region 0 is the dimmest region on chip S4, while Region 9 is the brightest.) The best fit abundances of Ne, S, Si, and Fe have significant gradients, but the best fit temperatures and ionization parameters (Tau) do not.

Fig. 11.— Same as Figure 10, but for the VMEKAL fits.

Fig. 12.— Top Panel: *Chandra* spectrum from the remnant's center (using the eighth rectangular segment from the left edge of chip 7), marked with crosses and spectrum from the thermally conductive (or entropy mixed) hydrocode model, marked by a histogram. The residuals are also shown. The reduced χ^2 for the fit is 1.5. Middle Panel: *Chandra* spectrum from the remnant's center, marked with crosses, and spectrum from the non-conducting hydrocode model, marked by a histogram. The residuals are also shown. The reduced χ^2 for the fit is 5.1. Bottom Panel: *Chandra* spectrum from the remnant's center, marked with crosses, and spectrum from the non-conducting hydrocode model combined with a model for hot, recently ionized, evaporated material, marked by a histogram. The residuals are also shown. The reduced χ^2 for the fit is 2.2.

Fig. 13.— Fluxes of 0.7 to 2.2 keV emission, as a function of off-axis angle for a model plasma having the observed Ne, Mg, S, Si, and Fe gradients (solid histogram) and a model plasma having constant Ne, Mg, S, Si, and Fe abundances (dashed histogram). All other parameters (density, temperature, and normalization as a function of off-axis angle) are identical for these two models and were found by fitting VMEKAL models to the data. The contrast between these plots demonstrates that the observed metallicity gradient has contributed signficantly to the surface brightness gradient.

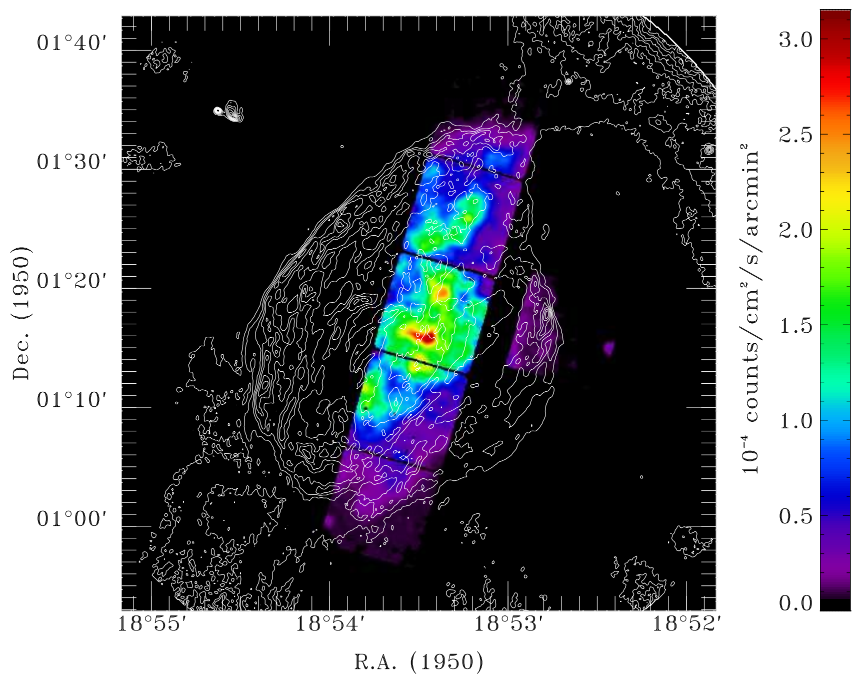
01°40′
01°30′
01°20′
01°10′
01°00′
Dec. (1950)
18°55′
18°54′
18°53′
18°52′
R.A. (1950)
3.0
2.5
2.0
1.5
1.0
0.5
0.0
10⁻⁴ counts/cm²/s/arcmin²

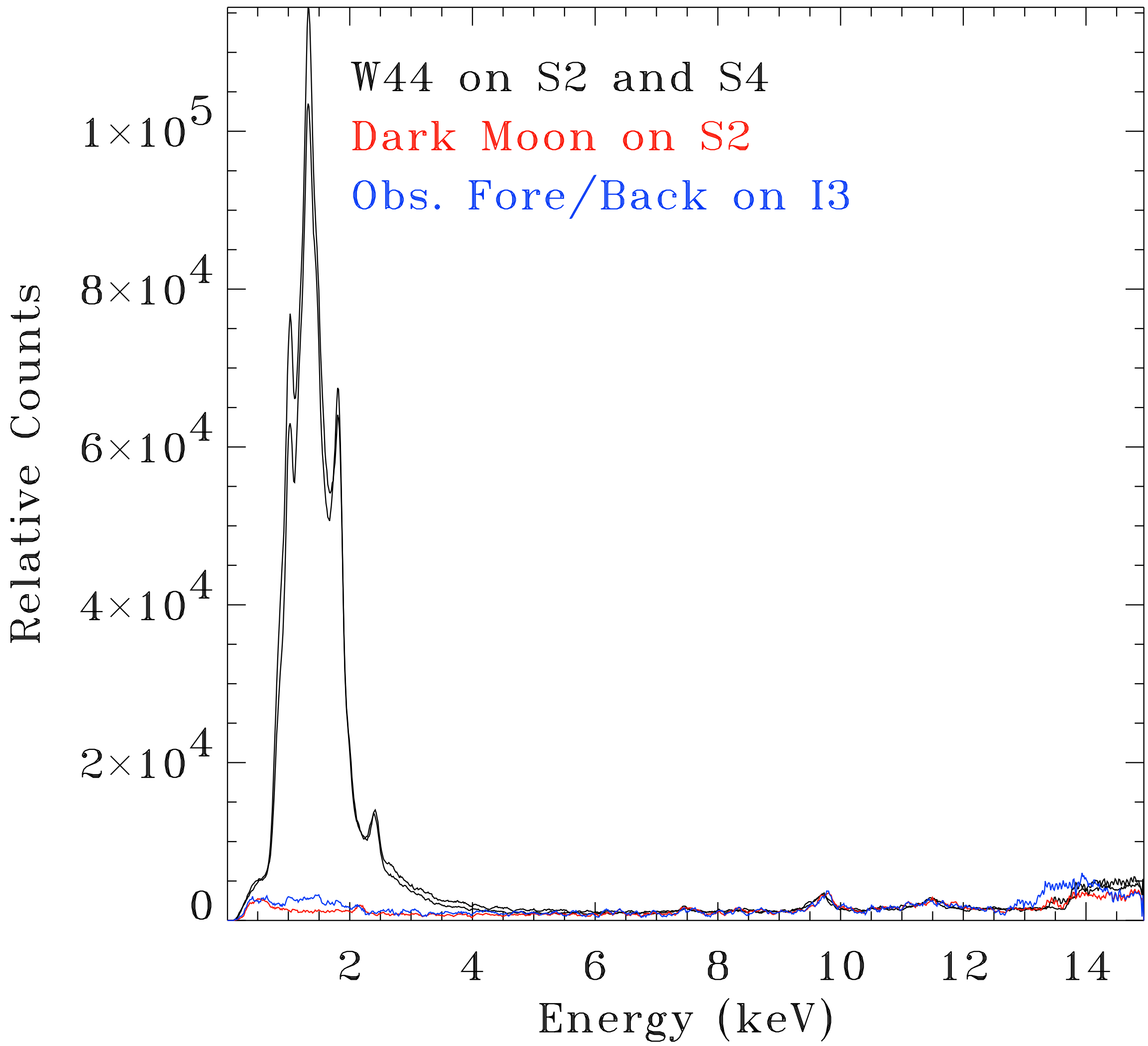
W44 on S2 and S4
Dark Moon on S2
Obs. Fore/Back on I3
Relative Counts
Energy (keV)
0
2×10^4
4×10^4
6×10^4
8×10^4
1×10^5
2
4
6
8
10
12
14

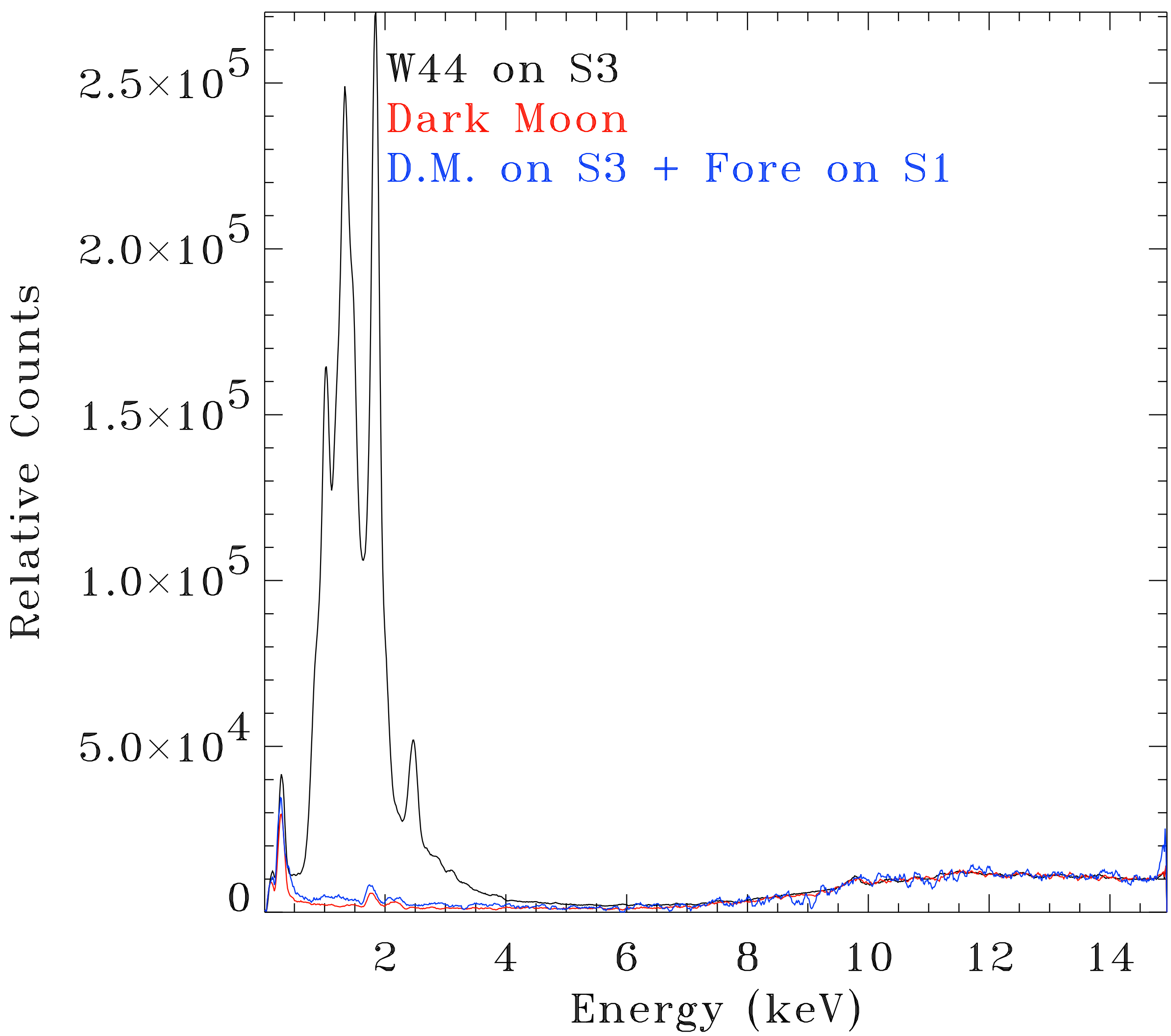
W44 on S3
Dark Moon
D.M. on S3 + Fore on S1
Relative Counts
2.5×10^5
2.0×10^5
1.5×10^5
1.0×10^5
5.0×10^4
0
2
4
6
8
10
12
14
Energy (keV)

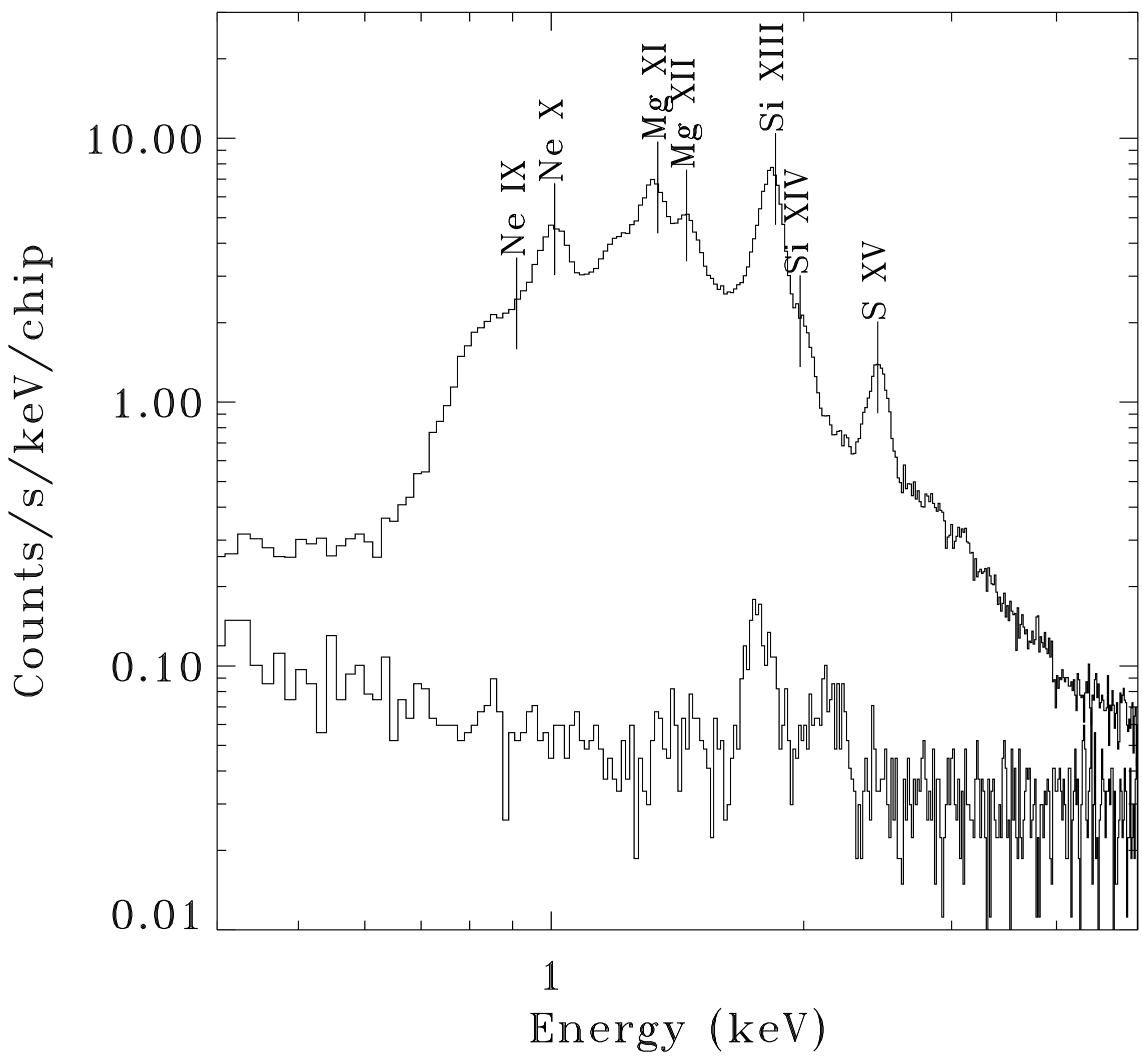
Ne IX
Ne X
Mg XI
Mg XII
Si XIII
Si XIV
S XV
10.00
1.00
0.10
0.01
Counts/s/keV/chip
1
Energy (keV)

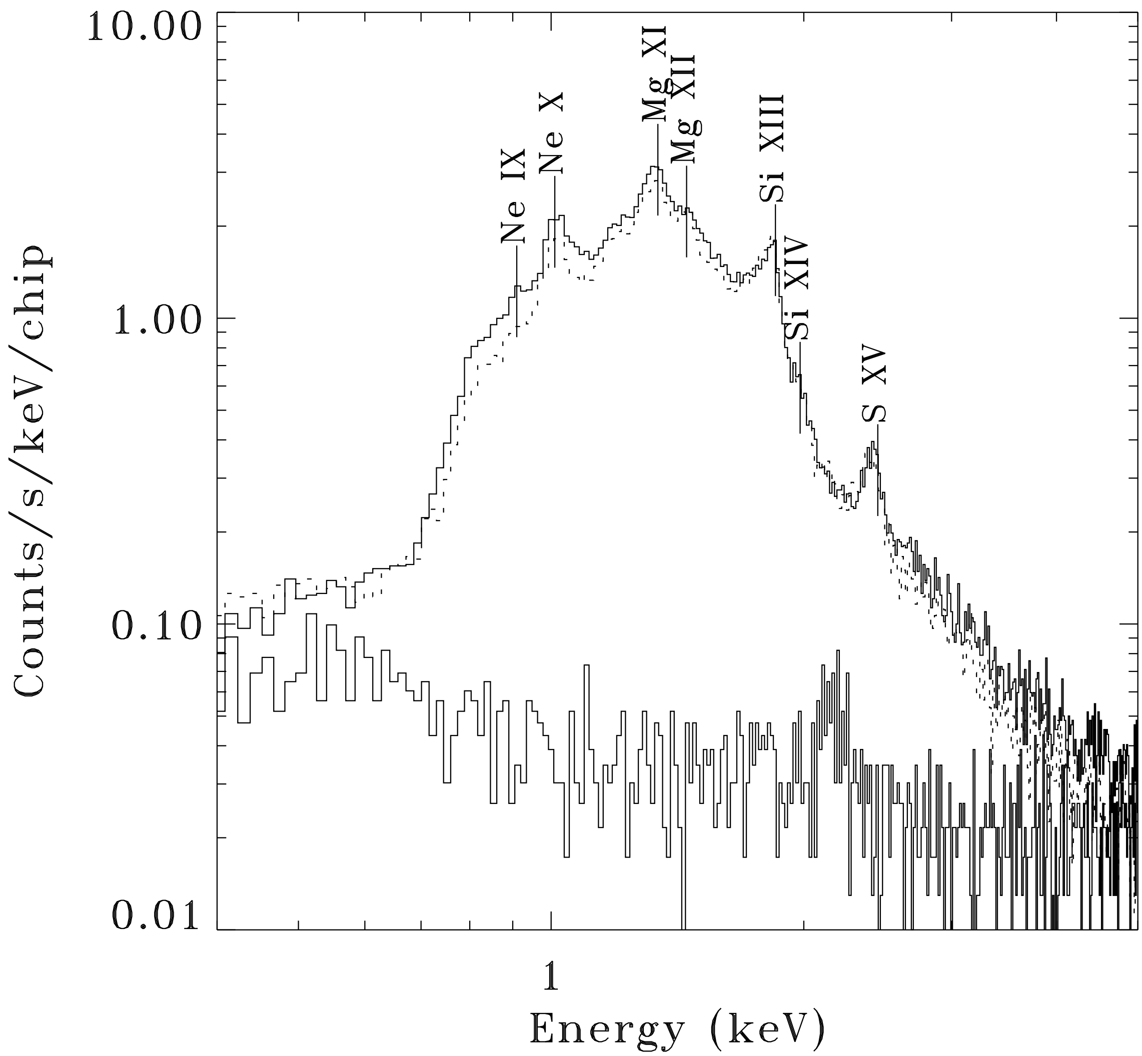
10.00
1.00
0.10
0.01
Counts/s/keV/chip
1
Energy (keV)
Ne IX
Ne X
Mg XI
Mg XII
Si XIII
Si XIV
S XV

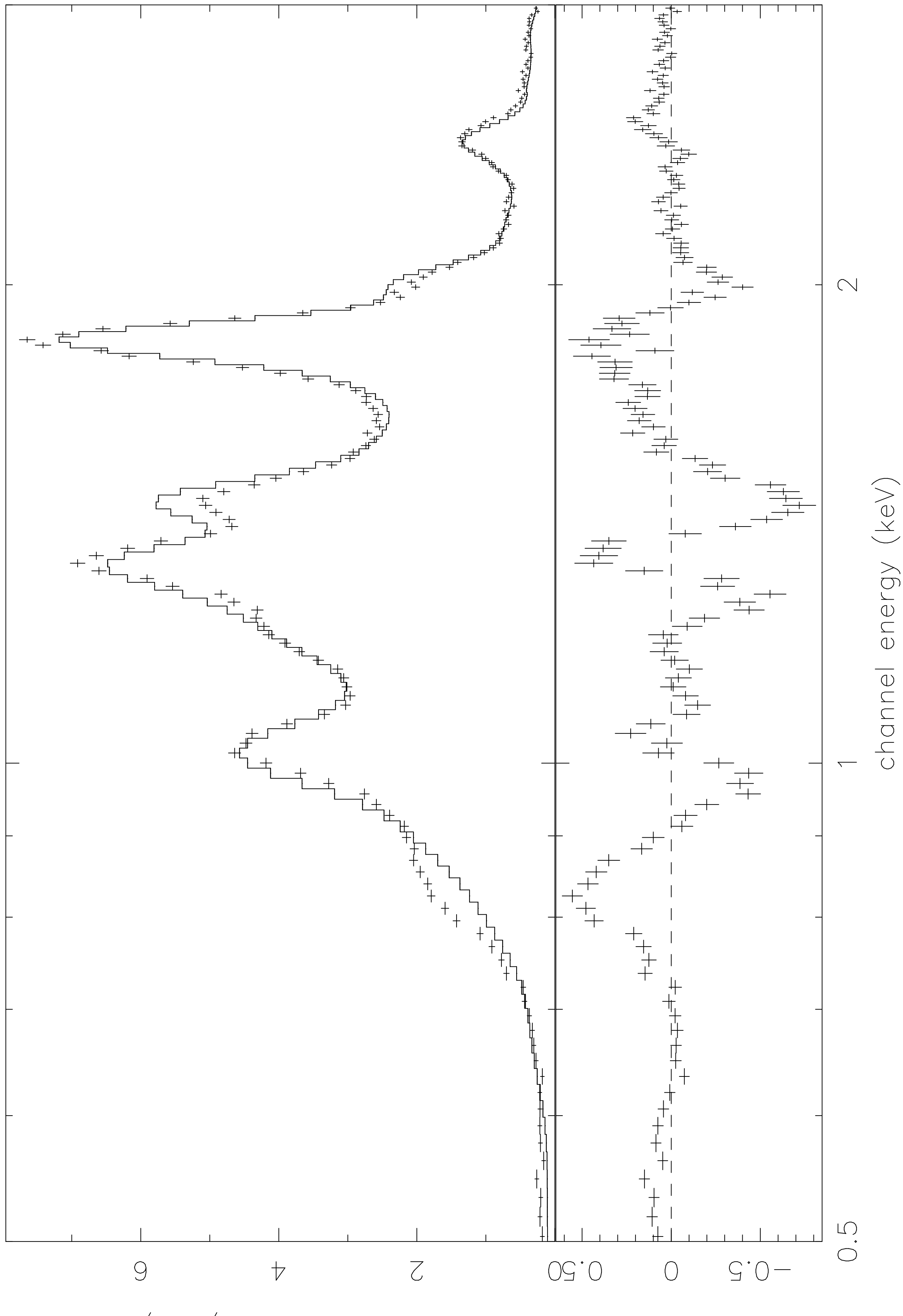
channel energy (keV)
0.5
1
2
6
4
2
0.50
0
−0.5

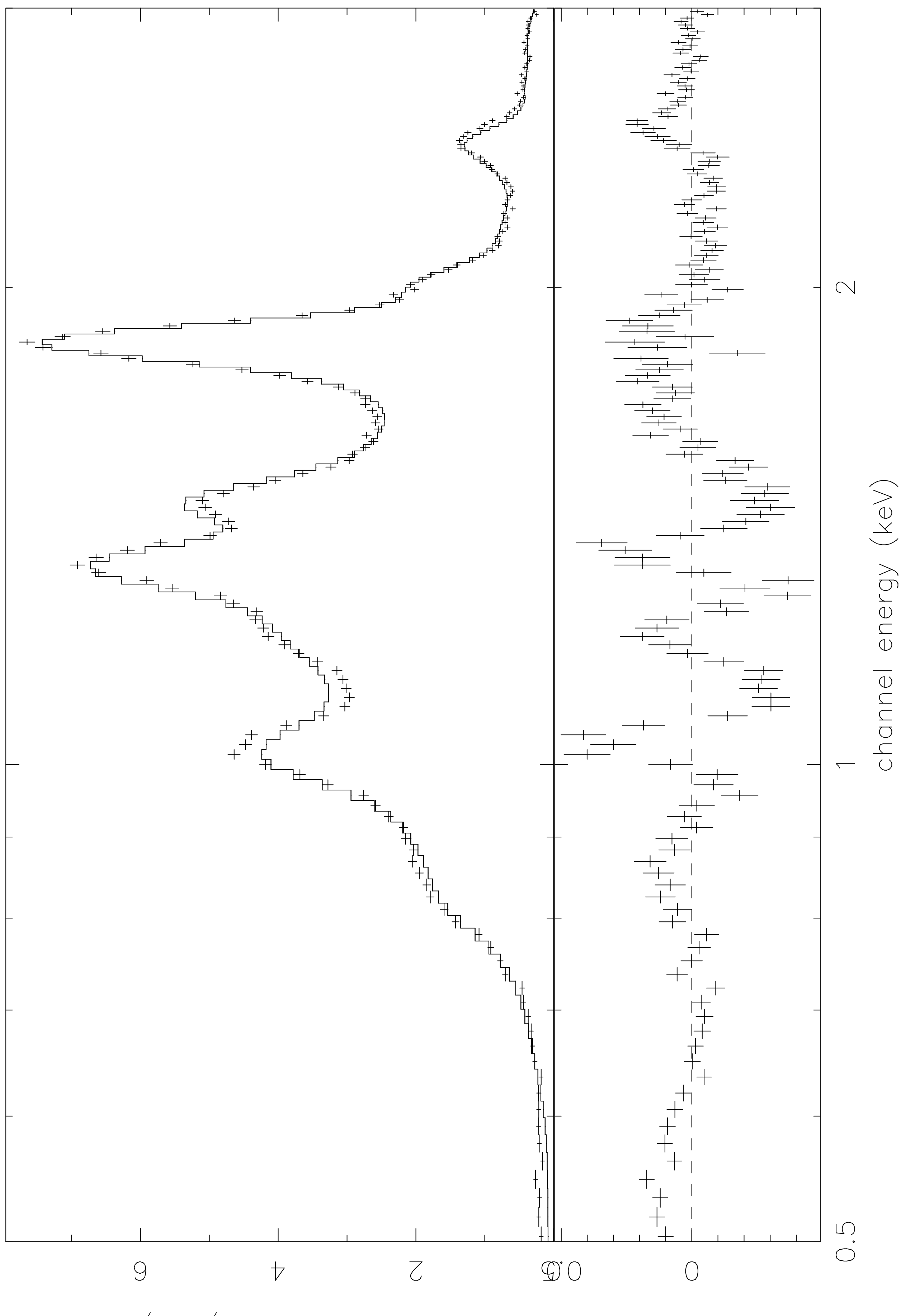
channel energy (keV)
0.5
1
2
0
2
4
6

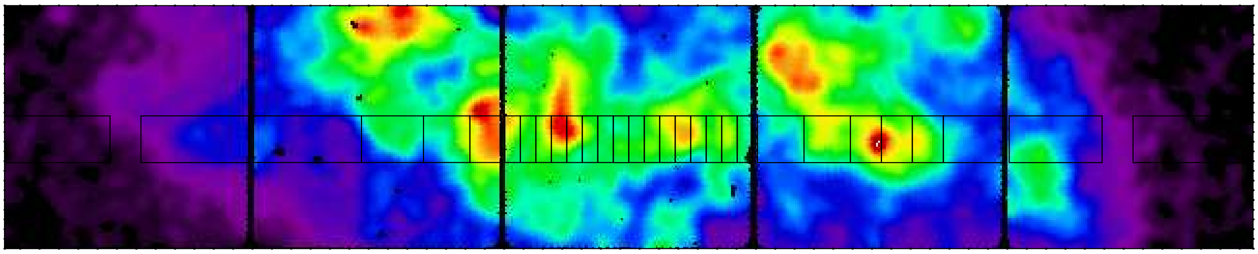

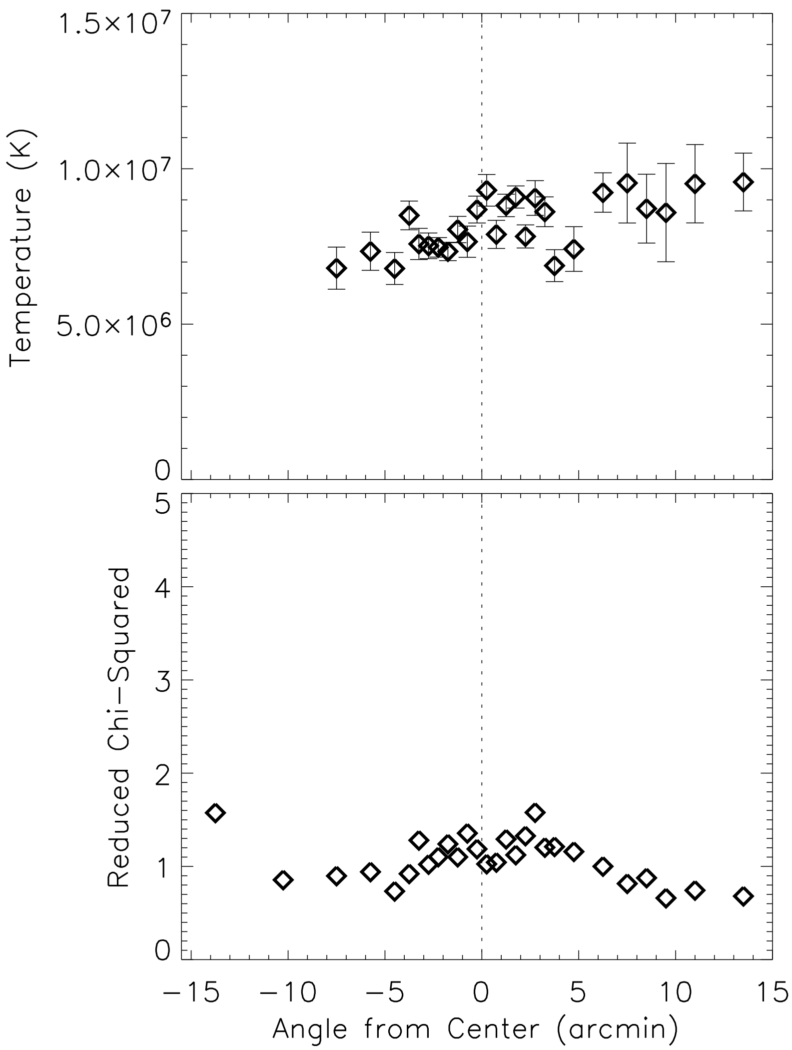

1.5×10^7
1.0×10^7
5.0×10^6
0
Temperature (K)
5
4
3
2
1
0
Reduced Chi–Squared
−15
−10
−5
0
5
10
15
Angle from Center (arcmin)

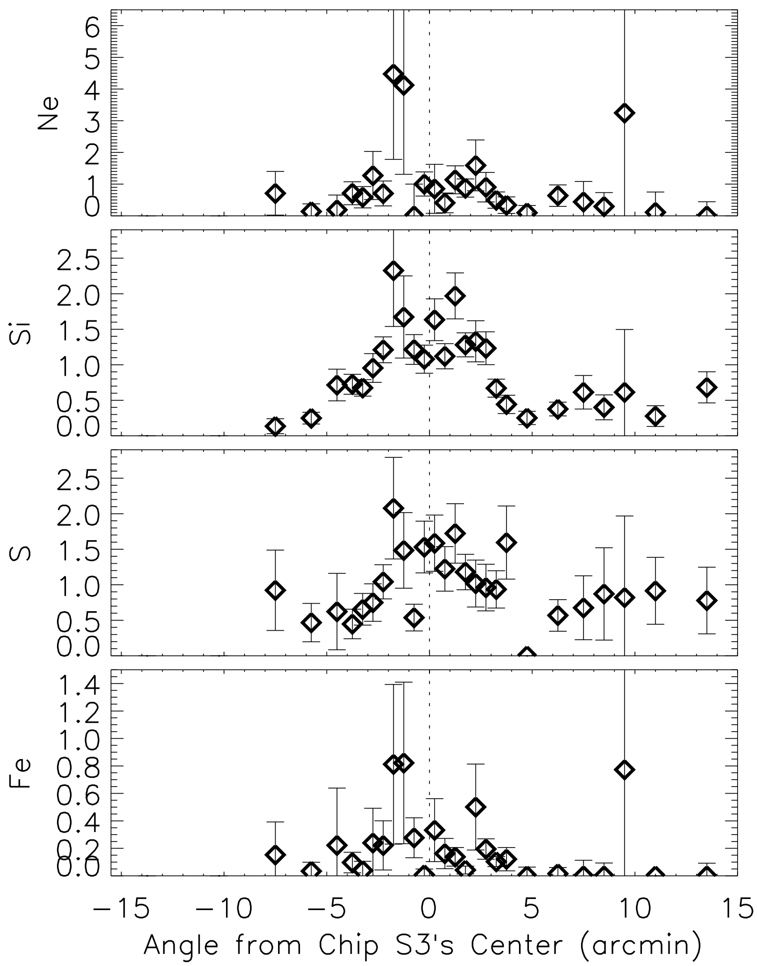

Ne
Si
S
Fe
Angle from Chip S3's Center (arcmin)

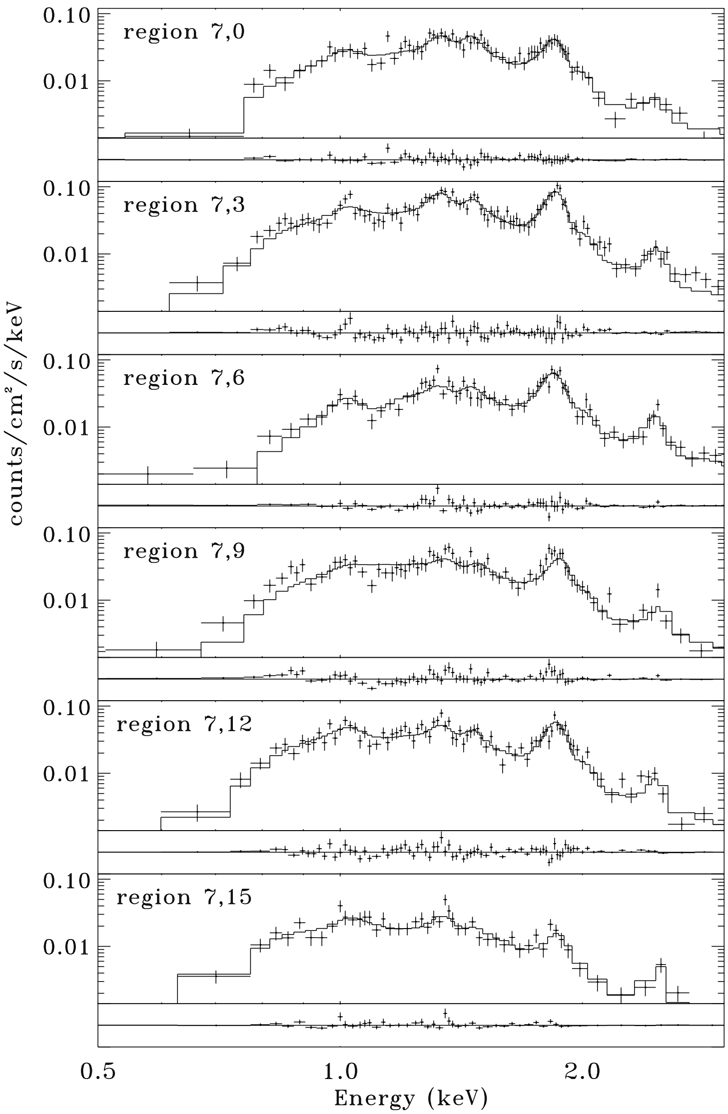
region 7,0
region 7,3
region 7,6
region 7,9
region 7,12
region 7,15
0.10
0.01
counts/cm²/s/keV
0.5
1.0
2.0
Energy (keV)

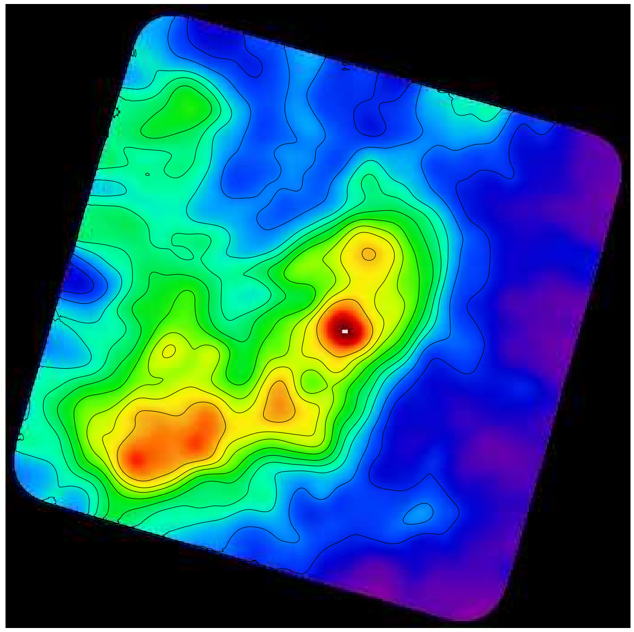

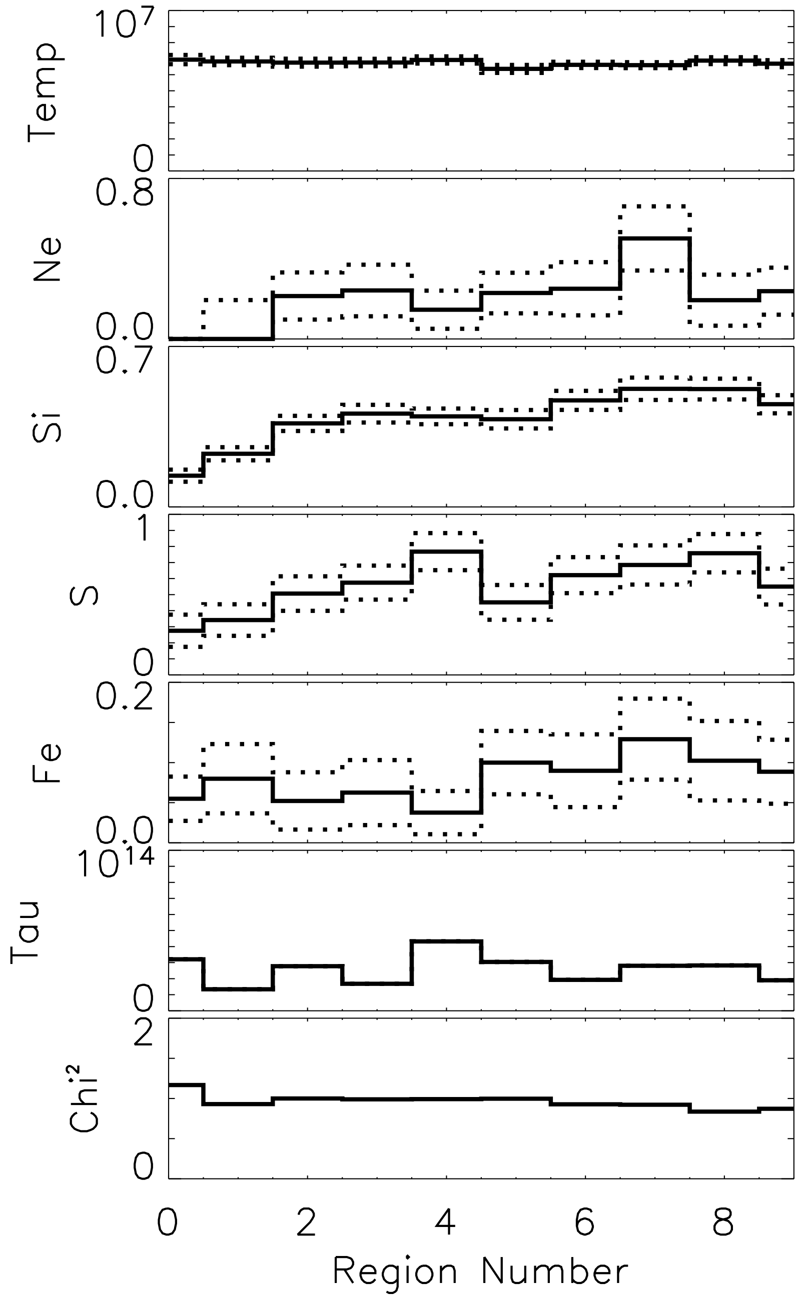

10^7
Temp
0
0.8
Ne
0.0
0.7
Si
0.0
1
S
0
0.2
Fe
0.0
10^{14}
Tau
0
2
Chi²
0
0
2
4
6
8
Region Number

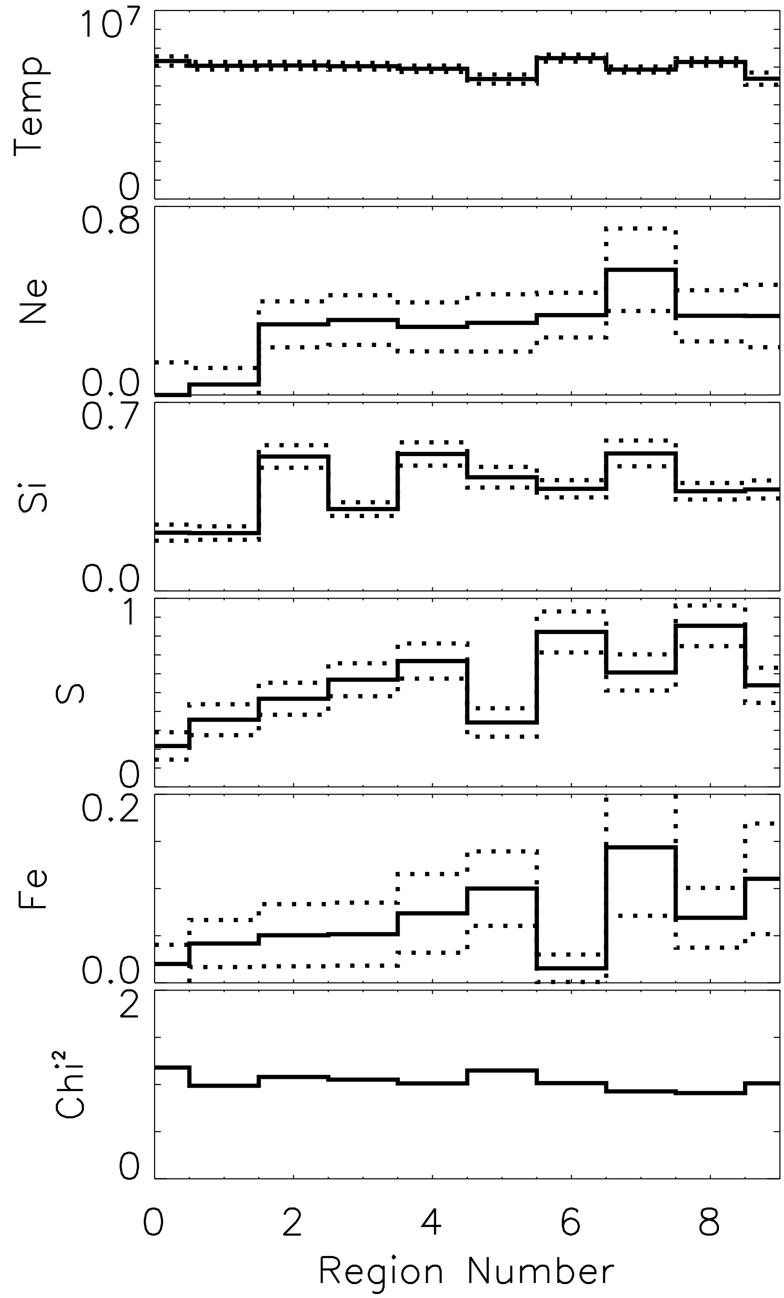

10^7
0
Temp
0.8
0.0
Ne
0.7
0.0
Si
1
0
S
0.2
0.0
Fe
2
0
Chi²
0
2
4
6
8
Region Number

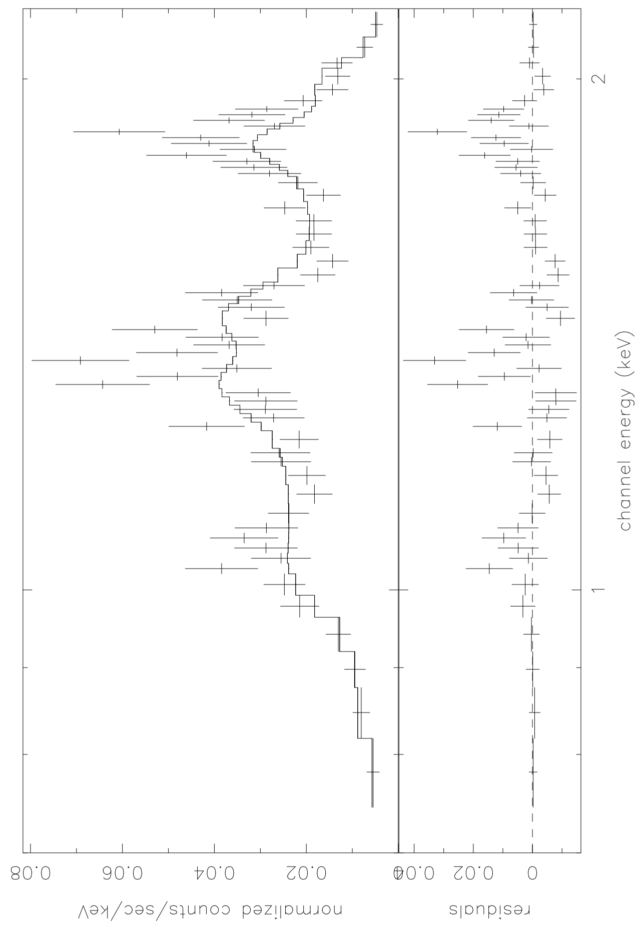
normalized counts/sec/keV
0.08
0.06
0.04
0.02
0.04
residuals
0.02
0
channel energy (keV)
1
2

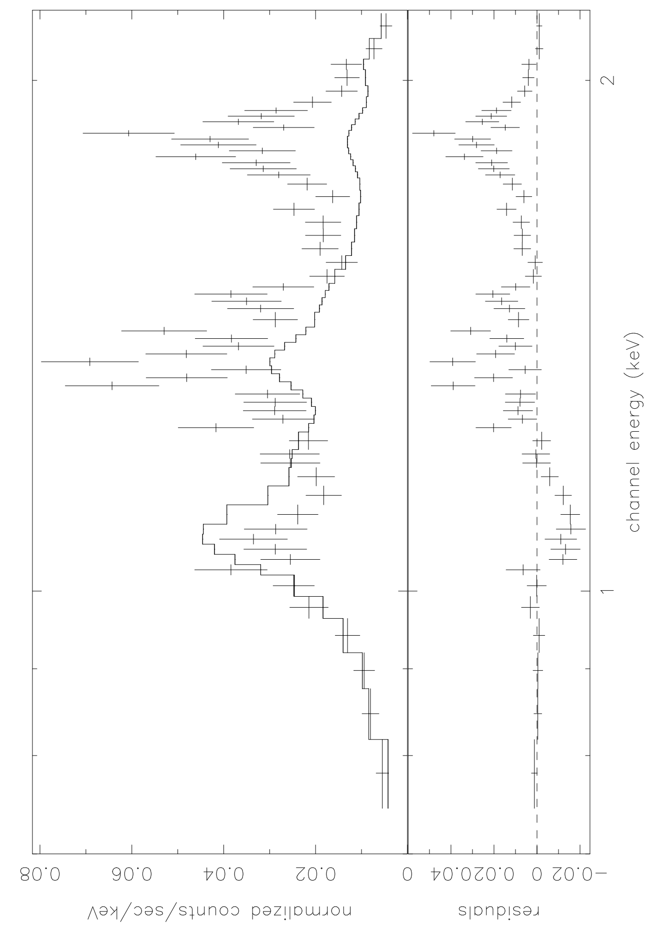
normalized counts/sec/keV
0.08
0.06
0.04
0.02
0
residuals
0.04
0.02
0
−0.02
channel energy (keV)
1
2

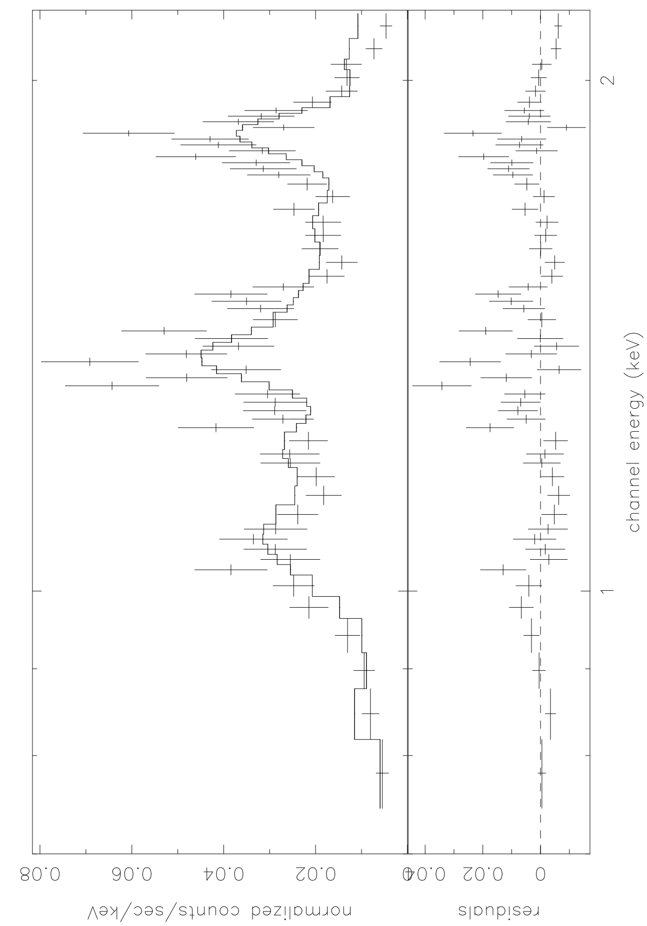
normalized counts/sec/keV
residuals
channel energy (keV)
0.08
0.06
0.04
0.02
0
0.04
0.02
0
1
2

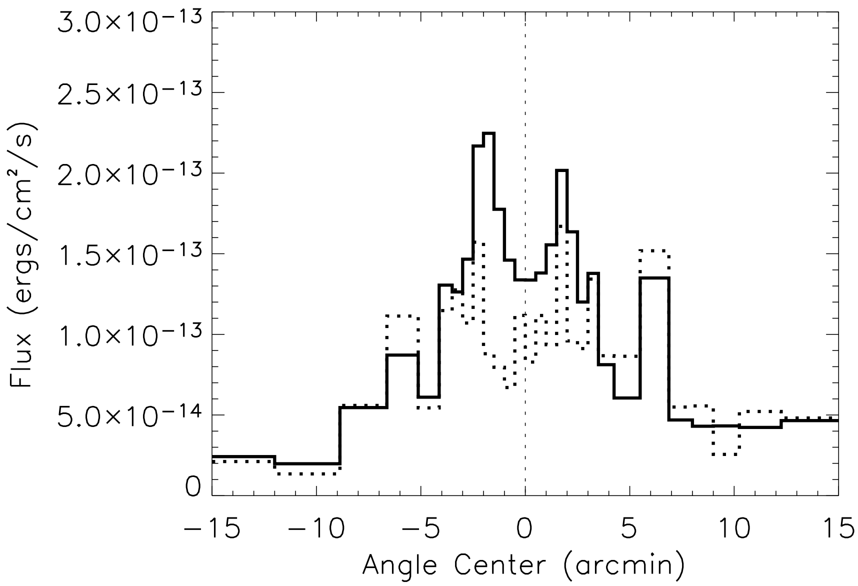
Flux (ergs/cm²/s)
3.0×10⁻¹³
2.5×10⁻¹³
2.0×10⁻¹³
1.5×10⁻¹³
1.0×10⁻¹³
5.0×10⁻¹⁴
0
−15
−10
−5
0
5
10
15
Angle Center (arcmin)